The annual cycle of gross primary production, net community production, and export efficiency across the North Pacific Ocean

Hilary I. Palevsky[1], Paul D. Quay[1], Deirdre E. Lockwood[1], and David P. Nicholson[2]

[1]School of Oceanography, University of Washington, Seattle, Washington, USA, [2]Marine Chemistry and Geochemistry Department, Woods Hole Oceanographic Institution, Woods Hole, Massachusetts, USA

Abstract We measured triple oxygen isotopes and oxygen/argon dissolved gas ratios as nonincubation-based geochemical tracers of gross oxygen production (GOP) and net community production (NCP) on 16 container ship transects across the North Pacific from 2008 to 2012. We estimate rates and efficiency of biological carbon export throughout the full annual cycle across the North Pacific basin (35°N–50°N, 142°E–125°W) by constructing mixed layer budgets that account for physical and biological influences on these tracers. During the productive season from spring to fall, GOP and NCP are highest in the Kuroshio region west of 170°E and decrease eastward across the basin. However, deep winter mixed layers (>200 m) west of 160°W ventilate ~40–90% of this seasonally exported carbon, while only ~10% of seasonally exported carbon east of 160°W is ventilated in winter where mixed layers are <120 m. As a result, despite higher annual GOP in the west than the east, the annual carbon export (sequestration) rate and efficiency decrease westward across the basin from export of $2.3 \pm 0.3\,\mathrm{mol\,C\,m^{-2}\,yr^{-1}}$ east of 160°W to $0.5 \pm 0.7\,\mathrm{mol\,C\,m^{-2}\,yr^{-1}}$ west of 170°E. Existing productivity rate estimates from time series stations are consistent with our regional productivity rate estimates in the eastern but not western North Pacific. These results highlight the need to estimate productivity rates over broad spatial areas and throughout the full annual cycle including during winter ventilation in order to accurately estimate the rate and efficiency of carbon sequestration via the ocean's biological pump.

1. Introduction

Export of biologically produced organic material in the ocean, known as the biological pump, plays an important role in regulating the global carbon cycle [*Volk and Hoffert*, 1985]. Photosynthesis by marine phytoplankton fixes CO_2 into organic carbon, some fraction of which is exported from the surface to the deep ocean and sequestered from the atmosphere on multiannual time scales. Global climate models project that anthropogenic climate change will decrease the strength of the biological pump over the 21st century [*Bopp et al.*, 2013], with potential feedback effects on climate and ocean biogeochemistry. Evaluating and predicting the role of the biological pump requires a mechanistic understanding of the processes controlling the rate and spatial patterns of photosynthetic primary production, as well as the mechanisms determining what fraction of fixed organic carbon is exported to the deep ocean rather than recycled at the surface. Accurate baseline measurements of current rates of primary production and biological carbon export are necessary to validate rates predicted by remote sensing algorithms and global climate models, as well as refine our understanding of the dominant processes controlling rates and efficiency of export.

The North Pacific is a region of particular interest for quantifying the rate and efficiency of the biological pump, as it is a major sink for atmospheric CO_2, absorbing $0.5\,\mathrm{Pg\,C\,yr^{-1}}$, ~25% of the total ocean CO_2 uptake [*Takahashi et al.*, 2009]. This regional carbon sink is driven largely by a band of strong CO_2 uptake between 30°N and 45°N [*Takahashi et al.*, 2002, 2009]. This band occurs at the transition between the subtropical and subarctic gyres and is defined both physically by multiple salinity fronts [*Roden*, 1991] and biologically by the transition zone chlorophyll front (TZCF) between lower chlorophyll subtropical waters to the south and higher-chlorophyll subarctic waters to the north [*Polovina et al.*, 2001; *Bograd et al.*, 2004]. A number of studies have attempted to quantify the contributions of biological carbon export to the North Pacific carbon sink, with recent work concluding that biological carbon export plays a role comparable to the combined effects of physical transport and solubility [*Chierici et al.*, 2006; *Ayers and Lozier*, 2012; *Lockwood*, 2013].

Productivity across the northern North Pacific has been described in most detail at two time series locations: the Kyodo North Pacific Time Series (KNOT; 44°N, 155°E) in the western subarctic gyre and Ocean Station Papa

(OSP; 50°N, 145°W) in the Alaskan gyre representing the nitrate-rich iron-limited subarctic. The western subarctic, represented by KNOT, is strongly influenced by the Kuroshio and Oyashio currents, which flow along the western boundary of the subtropical and western subarctic gyres, respectively, and join to form the Kuroshio Extension, while the eastern subarctic, represented by OSP, experiences weaker geostrophic transport. The deepest winter mixed layers (>200 m) are also found in the western basin, in bands directly to the north and south of the Kuroshio Extension [*Ohno et al.*, 2009]. Prior basin-wide comparisons of KNOT and OSP have observed a more pronounced seasonal cycle at KNOT featuring a spring diatom bloom, while OSP experiences a smaller-amplitude seasonal cycle with production dominated by small (<5 μm) cells year-round [*Harrison et al.*, 2004]. Measurements beyond these time series sites show, however, that the high carbon uptake region of the North Pacific is not fully represented by these locations. Meridional transects spanning spring through fall have found elevated primary production and carbon export at the TZCF [*Howard et al.*, 2010; *Juranek et al.*, 2012; *Lockwood et al.*, 2012], indicating the importance of including the full spatial variability across the North Pacific in basin-scale estimates.

Nonincubation-based dissolved gas tracers provide the means to estimate primary production and organic carbon export across broad spatial and temporal scales. The triple oxygen isotopic (TOI) composition of dissolved oxygen traces photosynthetic gross oxygen production (GOP) [*Luz and Barkan*, 2000; *Juranek and Quay*, 2013], and O_2/Ar dissolved gas ratios trace net community production (NCP) [*Emerson et al.*, 1991]. NCP represents the strength of the biological pump, while the fraction of GOP that contributes to NCP (NCP/GOP ratio) represents its efficiency. Dissolved gas productivity tracers integrate over the ~1–2 week residence time of gases in the surface mixed layer, facilitating capture of episodic production events, and can be applied using only surface samples, enabling underway sampling on vessels of opportunity. Repeated sampling of these and other tracers using container ship platforms have provided basin-wide estimates over the full annual cycle of both GOP and NCP in the North Atlantic [*Quay et al.*, 2012; *Ostle et al.*, 2014], GOP across the tropical and subtropical Pacific [*Juranek and Quay*, 2010], and NCP across the North Pacific [*Wong et al.*, 2002a; *Chierici et al.*, 2006; *Lockwood*, 2013].

In this study, we estimate GOP and NCP from TOI and O_2/Ar samples collected on 16 basin-wide crossings of the North Pacific on commercial container ships. Our approach allows us to estimate rates and efficiency of biological carbon export throughout the full annual cycle across the entire North Pacific basin from 142°E to 125°W and 35°N to 50°N. These are the first basin-wide observational estimates of primary production throughout the annual cycle in the North Pacific and the first simultaneous application of TOI and O_2/Ar on a vessel of opportunity to estimate annual GOP, NCP, and export efficiency on a basin-wide scale. We find that despite higher seasonal GOP and NCP in the western regions of the North Pacific in the spring through fall, annual carbon export rates and efficiency are greater in the east than the west due to deeper winter ventilation in the west.

2. Methods

2.1. Sample Collection and Measurement

Samples for TOI and O_2/Ar analysis were collected from shipboard seawater intake (10 m depth) on 16 basin-wide transects of the North Pacific between Hong Kong and Long Beach, California, onboard the M/V *OOCL Tianjin* and the M/V *OOCL Tokyo* between October 2008 and December 2012 (Figure 1). Samples were collected into prevacuated 500 mL flasks every ~2.5° longitude across the basin following the procedures of *Emerson et al.* [1999]. Sea surface temperature (SST) and salinity at the time of sample collection were determined using a Sea-Bird Electronics SBE45 thermosalinograph installed in the ship's seawater intake. To prevent biofouling that could cause respiration in the ship's seawater lines and contaminate O_2/Ar measurements [*Juranek et al.*, 2010], intake lines between the anticorrosive sea chest and the sampling port were purged with bleach and freshwater between every cruise. Additional depth profile samples for TOI and O_2/Ar analysis were collected from a late winter cruise in February–March 2013 onboard the R/V *Melville* in the western North Pacific from Niskin bottles tripped at depths ranging from the surface to 300 m, chosen to capture both mixed layer and thermocline properties (Figure 1).

In the laboratory, dissolved gas samples were equilibrated at room temperature for 24 h and then drained under vacuum to remove seawater. Oxygen and argon were cryogenically extracted and separated from the remainder of the dissolved gas mixture following the procedures of *Juranek and Quay* [2005]. Samples were subsequently analyzed on a Finnegan MAT 253 isotope ratio mass spectrometer using 75 paired measurements of masses 32,
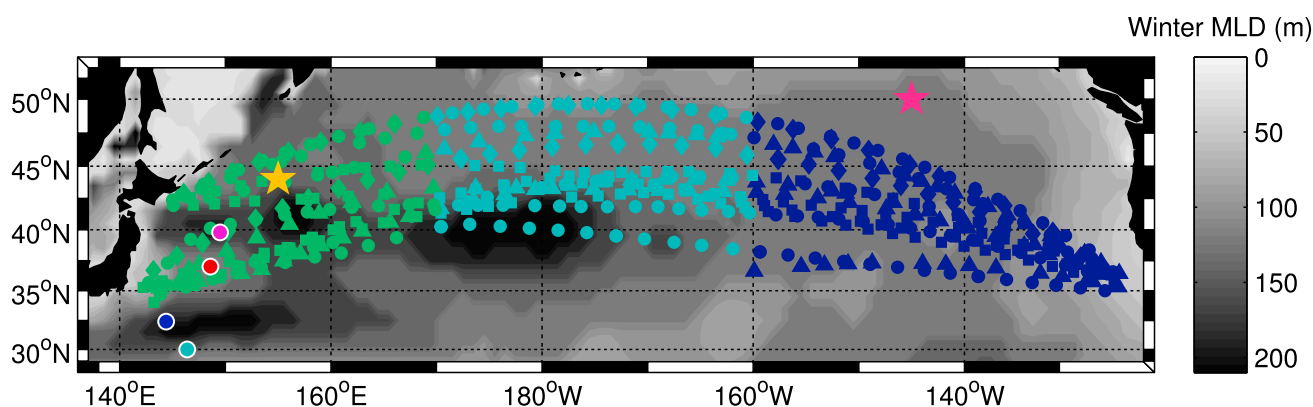
Figure 1. Mixed layer discrete samples collected on 16 basin-wide transects of the North Pacific between 2008 and 2012 are divided for analysis into three regions: the Kuroshio (green), the Western region (light blue), and the Eastern region (dark blue). The annual cycle is divided by season: spring (March–May, triangles), summer (June–August, diamonds), fall (September–November, squares), and winter (December–February, circles). The four colored circles outlined in white indicate depth profile samples collected in late winter 2013. Stars indicate time series stations at KNOT (yellow) and OSP (pink), for comparison to previous measurements. Sample locations are overlain on climatological maximum winter mixed layer depth (MLD), calculated from World Ocean Atlas data (see Table 1 for details).

33, and 34 alternating with measurements of an internal standard to determine $\delta^{17}O$ and $\delta^{18}O$, followed by measurements of masses 32 and 40 on a single collector to determine O_2/Ar. Reported values for $\delta^{17}O$ and $\delta^{18}O$ are corrected for the experimentally determined dependence on both the sample size, as described by *Stanley et al.* [2010], and the sample O_2/Ar ratio. Measurement uncertainty for each sample batch was determined based on daily air standards, yielding a mean uncertainty (1σ) of 6.9 per meg for $^{17}\Delta$ (defined in section 2.3, equation (1)), 0.020‰ for $\delta^{17}O$, 0.036‰ for $\delta^{18}O$, and 0.036 for O_2/Ar. Air-equilibrated water standards collected at both 4°C and room temperature (20–22°C) measured in a series of experiments ($n = 149$) throughout the course of this study yield $^{17}\Delta_{eq}$ of $8 \pm 1 \left(\frac{2\sigma}{\sqrt{n}} \right)$ per meg, with no temperature dependence, consistent with the value of 8 per meg reported by *Reuer et al.* [2007] and *Stanley et al.* [2010].

2.2. Regional Divisions

We divide the North Pacific basin into three regions for analysis: the Kuroshio, west of 170°E, influenced by the Kuroshio, Oyashio, and Kuroshio Extension currents; the Western region, between 170°E and 160°W; and the Eastern region, east of 160°W (Figure 1). This regional division scheme enables analysis of the east-west basin-wide trends previously identified in comparisons of the western subarctic and Alaskan gyres [*Harrison et al.*, 2004], and the influence of deeper winter mixed layers in the western basin (Figure 1) [*Ohno et al.*, 2009]. While these large regions encompass multiple physical and biological fronts across the transition between the subarctic and subtropics which have led previous studies to create finer regional subdivisions [e.g., *Wong et al.*, 2002a; *Chierici et al.*, 2006], our coarser regional division scheme increases sampling density within each region, which yields more accurately described annual cycles.

All terms in the GOP and NCP budgets (section 2.3) are calculated for each discrete sample and then compiled to calculate mean values for each budget term for each region and season. To evaluate potential for sampling bias in the three defined regions, we apply satellite observations of SST and chlorophyll as proxies for spatial and temporal variability in GOP and NCP, supported by the use of SST and chlorophyll in satellite-based algorithms for productivity and export efficiency [e.g., *Behrenfeld and Falkowski*, 1997; *Laws et al.*, 2000; *Dunne et al.*, 2005]. Moderate Resolution Imaging Spectroradiometer (MODIS) SST and chlorophyll ($1/6° \times 1/6°$ monthly data provided by the Oregon State Ocean Productivity group, http://www.science.oregonstate.edu/ocean.productivity) seasonal mean values for all grid points within each region sampled continuously from 2008 to 2012 were compared with seasonal mean values determined only from the times and cruise track locations where discrete samples were collected (Figure 2). Overall, the SST and chlorophyll comparison between the complete coverage and cruise track-sampled locations shows that the annual cycle in all three regions is generally well represented. There is some discrepancy in spring chlorophyll and summer SST in the Western region and spring SST in the Kuroshio region, as well as high spatial variability in Kuroshio region chlorophyll in spring and fall. We use this comparison as a means to quantify the degree of sampling bias in each region and season (see section 2.5).
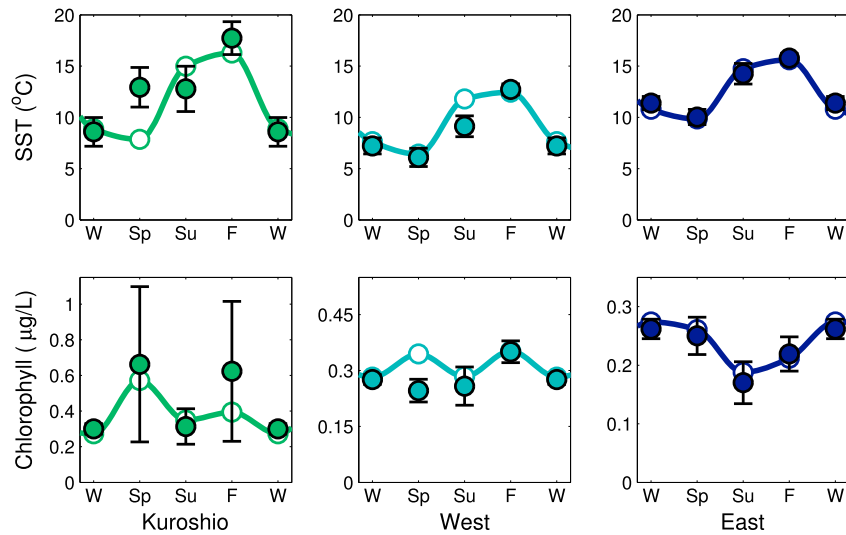
Figure 2. The seasonal cycle of (top) sea surface temperature (SST) and (bottom) chlorophyll in each region, from MODIS satellite data. Open circles connected by solid lines show mean values over all points in the region in all three months composing each season in every year 2008–2012. Filled circles show mean values sampled only at the locations and times when discrete samples were collected during this study. Error bars represent twice the standard error of the mean (error bars not shown are smaller than the marker size). Discrepancies between the solid and open circles reflect undersampling bias. Note the varying y axis for chlorophyll plots.

2.3. Triple Oxygen Isotope (TOI) and O_2/Ar Budget Approaches to Estimate GOP and NCP

Estimation of GOP and NCP rates based on measured TOI and O_2/Ar, respectively, requires construction of surface mixed layer budgets accounting for tracer sources and sinks. Both tracers are often interpreted by assuming steady state conditions and negligible physical tracer flux due to mixing or advection. However, modeling and observational studies have demonstrated that these assumptions are not always valid and can introduce large errors [*Hamme et al.*, 2012; *Nicholson et al.*, 2012, 2014; *Jonsson et al.*, 2013]. In this study, we construct budgets for both TOI and O_2/Ar that account for physical supply and nonsteady state conditions to more accurately estimate GOP and NCP throughout the full annual cycle.

The TOI approach, described in detail elsewhere [*Luz and Barkan*, 2000; *Juranek and Quay*, 2013], enables estimates of GOP based on isotopic differentiation between dissolved oxygen in seawater produced during photosynthesis and dissolved oxygen contributed by atmospheric equilibration. The TOI approach requires measurements of both $\delta^{17}O$ and $\delta^{18}O$, which are commonly combined to define a single term, $^{17}\Delta$ [*Luz and Barkan*, 2005]:

$$^{17}\Delta \equiv 10^6 \left[\log\left(1 + \frac{\delta^{17}O}{10^3}\right) - \lambda \log\left(1 + \frac{\delta^{18}O}{10^3}\right) \right] \tag{1}$$

Oxygen in the atmosphere is depleted in ^{17}O due to mass-independent photochemical reactions in the stratosphere and is defined as a standard such that $^{17}\Delta_{atmos} = 0$ per meg, whereas oxygen produced photosynthetically from seawater yields $^{17}\Delta_p = 250$ per meg [*Luz and Barkan*, 2000; *Lämmerzahl*, 2002]. The $^{17}\Delta$ is defined to be insensitive to removal of oxygen through respiration through the empirically determined choice of $\lambda = 0.518$, which maintains a constant $^{17}\Delta$ even while respiration consumes O_2 and enriches both $\delta^{17}O$ and $\delta^{18}O$ [*Luz and Barkan*, 2005].

The mixed layer budget for TOI, accounting for the influences of air-sea gas exchange, nonsteady state TOI concentrations, and physical supply of TOI, can be solved to determine GOP:

$$\text{GOP} \approx \frac{k[O_2]_{eq}\left(^{17}\Delta_{ml} - ^{17}\Delta_{eq}\right) + z_{ml}[O_2]_{ml}\left(\frac{\partial(^{17}\Delta_{ml})}{\partial t} - \left[\frac{\partial(^{17}\Delta_{ml})}{\partial t}\right]_{phys}\right)}{\left(^{17}\Delta_P - ^{17}\Delta_{ml}\right)} \tag{2}$$

where k is the air-sea gas transfer velocity (m d^{-1}), z_{ml} is the mixed layer depth (m), and the subscripts P, eq, and ml represent photosynthetic end-member [*Luz and Barkan*, 2009], air-equilibrated end-member

($^{17}\Delta_{eq} = 8$ per meg, section 2.1; $[O_2]_{eq}$ from *Garcia and Gordon* [1992]), and measured values, respectively, for mixed layer dissolved oxygen. Recent work has demonstrated the importance of calculating GOP directly from $\delta^{17}O$ and $\delta^{18}O$ rather than from $^{17}\Delta$ [*Kaiser*, 2011; *Prokopenko et al.*, 2011]. We use this more rigorous approach to the GOP budget in equation (2) but present measured TOI using the more intuitive $^{17}\Delta$.

The O_2/Ar approach enables estimates of NCP by isolating biological effects on oxygen supersaturation from effects of bubble injection and temperature-driven solubility changes, which affect argon similarly to oxygen [*Craig and Hayward*, 1987; *Emerson et al.*, 1991]. Biological oxygen supersaturation from O_2/Ar is defined as

$$\Delta O_2/Ar = \frac{(O_2/Ar)_{ml}}{(O_2/Ar)_{eq}} - 1 \tag{3}$$

where $(O_2/Ar)_{ml}$ is the measured ratio of dissolved oxygen to argon in the mixed layer and $(O_2/Ar)_{eq}$ is the equilibrium ratio determined by the temperature- and salinity-dependent solubility of both gases [*Garcia and Gordon*, 1992; *Hamme and Emerson*, 2004]. In a system at steady state with negligible physical supply, $\Delta O_2/Ar > 0$ indicates that oxygen is supersaturated due to net autotrophic conditions, whereas $\Delta O_2/Ar < 0$ indicates net heterotrophic conditions.

A surface mixed layer budget of O_2/Ar accounting for nonsteady state conditions, air-sea biological oxygen flux, and physical supply of oxygen and argon can be used to estimate NCP:

$$NCP = k[O_2]_{eq}\Delta O_2/Ar + \frac{\partial(\Delta O_2/Ar)}{\partial t}z_{ml}[O_2]_{eq} - z_{ml}\left(\frac{\partial O_2}{\partial t}_{phys} - (O_2/Ar)_{eq}\frac{\partial Ar}{\partial t}_{phys}\right) \tag{4}$$

The derivation of equation (4) from separate oxygen and argon budgets, following the approach of *Howard et al.* [2010], is given in the supporting information.

Note that the GOP and NCP budgets (equations (2) and (4)) can both be expressed in simplified form as

$$NCP \text{ or } GOP = \text{Air-sea flux} + \text{Non-steady state} - \text{Physical supply} \tag{5}$$

In conditions where the nonsteady state and physical supply terms are negligible, as has often been assumed in previous applications of the TOI and $\Delta O_2/Ar$ methods, GOP and NCP are equal to their respective air-sea flux terms. Calculation details for both tracer budgets, broken down based on the three right-hand side (RHS) components of equation (5), are provided below. All RHS terms in both budgets are calculated for each discrete sample and then compiled to calculate mean values for each term for each region and season.

2.3.1. Air-Sea Flux

Air-sea tracer flux for both GOP (equation (2)) and NCP (equation (4)) depends on the air-sea gas transfer velocity (k) over the residence time of dissolved oxygen in the surface mixed layer in addition to tracer measurements. Daily wind speed data from the NOAA National Climactic Data Center's multiple-satellite Blended Sea Winds product (https://www.ncdc.noaa.gov/oa/rsad/air-sea/seawinds.html) were used to calculate k for the time and location of each discrete sample following the *Nightingale et al.* [2000] relationship between k and wind speed and the *Reuer et al.* [2007] weighting scheme.

Uncertainty in the air-sea gas exchange rate is estimated by assuming that the majority of uncertainty results from the parameterized relationship between gas exchange rate (k) and wind speed and that the spread between the air-sea gas exchange rates calculated from the *Liss and Merlivat* [1986] and *Wanninkhof* [1992] equations represents 95% of the variability ($\pm 2\sigma$) in k [*Palevsky et al.*, 2013], yielding a mean uncertainty in k of $\pm 14\%$ over all discrete sample locations in the data set.

2.3.2. Nonsteady State Terms

Seasonal GOP and NCP budget nonsteady state terms in equations (2) and (4) are determined from discrete sample-specific tracer time rate of change tendencies and estimates of the mixed layer depth (z_{ml}, Table 1) and $[O_2]_{eq}$, compiled to compute the mean nonsteady state term for each region and season. To determine the tracer time rate of change tendencies, all surface mixed layer TOI and O_2/Ar data for each region are compiled into a single composite year, with the seasonal cycle of TOI and O_2/Ar determined by fitting simple harmonic functions using a least squares approach. The derivatives of these harmonic fits for the day of the year corresponding to collection of each discrete sample are used to calculate the time rate of change tendency of mixed layer TOI and O_2/Ar, $\frac{\partial(^{17}\Delta_{ml})}{\partial t}$ and $\frac{\partial(\Delta O_2/Ar)}{\partial t}$.

Table 1. Data Sources for NCP Budget Physical Supply Correction Terms

Parameter	Data Source	Spatial Resolution	Time Resolution
Oxygen (O_2), temperature (T), salinity (S)	World Ocean Atlas 2013 (WOA) (https://www.nodc.noaa.gov/OC5/woa13)	1° × 1°	Monthly climatology (data from 1955 to 2012)
Argon (Ar)	Calculated from WOA T and S [*Hamme and Emerson*, 2004]	1° × 1°	Monthly climatology (data from 1955 to 2012)
Mixed layer depth (z_{ml})	0.125 kg m^{-3} density increase from the surface, from WOA T and S [*Monterey and Levitus*, 1997]	1° × 1°	Monthly climatology (data from 1955 to 2012)
Ekman transport ($\mathbf{u_{Ek}}$)[a]	U.S. Navy Fleet Numerical Meteorology and Oceanography Center data derived from synoptic surface pressure analyses (http://coastwatch.pfeg.noaa.gov/erddap/griddap/erdlasFnWPr.html)	1° × 1°	Monthly climatology (data from 2008 to 2012)
Geostrophic transport ($\mathbf{u_{Geo}}$)	Ssalto/Duacs absolute geostrophic velocity data from satellite altimetry, distributed by Aviso (http://www.aviso.altimetry.fr/en/data/products/sea-surface-height-products/global.html)	1/4° × 1/4°, regridded to 1° × 1°	Monthly climatology (data from 2008 to 2012)
Ekman-driven upwelling ($\mathbf{w_{Ek}}$)[b]	Horizontal divergence of mass due to Ekman transport ($\mathbf{u_{Ek}}$, above)	1° × 1°	Monthly climatology (data from 2008 to 2012)
Vertical diffusivity at the base of the mixed layer (K_z)	Winter/spring K_z determined by assuming winter NCP = 0. Summer/fall K_z scaled down from winter/spring values based on seasonal cycle observed at KEO and OSP [*Cronin et al.*, 2015].[c]	Regional	Seasonal climatology

[a]When the Ekman depth was deeper than the mixed layer, transport was scaled to only include Ekman transport within the mixed layer.
[b]When the vertical velocity is downward (downwelling), there is no effect on the mixed layer budget.
[c]Factors to scale winter/spring K_z for summer/fall are 0.1, 0.2, and 0.5 in the Kuroshio, Western, and Eastern regions, respectively, chosen based on the observed seasonal cycle amplitude at the Kuroshio Extension Observatory (KEO, 32.4°N, 144.6°E) and OSP [*Cronin et al.*, 2015]. Eastern region winter NCP is > 0 even when K_z = 0, so winter/spring K_z was chosen as 2.0×10^{-5} m^2 s^{-1}, twice background diffusivity.

2.3.3. Physical Supply Terms

Physical supply terms in the GOP and NCP budgets account for the influence on mixed layer TOI and O_2/Ar from horizontal advection due to geostrophic and Ekman transport, vertical advection from Ekman-driven upwelling, and vertical supply from entrainment and diffusive mixing. Estimating these terms requires knowledge of both the physical transport fields and the tracer spatial gradients in the ocean. For TOI, insufficient observational data exist to constrain tracer gradients, so the physical supply terms were estimated from the output of a global ocean model that included TOI (see section 2.3.3.1). For O_2/Ar, climatological O_2 gradients were used to estimate physical supply of O_2/Ar in the NCP budget (see section 2.3.3.2).

2.3.3.1. Physical Supply Term in the GOP Budget

The physical supply contribution to the GOP budget was estimated using output from a global ocean model (Parallel Ocean Program of the Community Earth System Model version 1.1.1, CESM) run at a nominal 1° resolution and modified to explicitly include oxygen isotopogues to simulate the TOI system. The TOI simulations used here have been previously described in detail by *Nicholson et al.* [2014]. Model diagnostic tracers for lateral and vertical advective and mixing fluxes were extracted at the location and sampling month of each discrete sample and used to determine the individual contributions to the GOP budget from upwelling, horizontal advection, and vertical supply (which encompasses both entrainment and diffusive vertical mixing).

To normalize for discrepancies in the spatial and temporal patterns of surface mixed layer TOI between the model and observations, the physical supply term calculated from model output was applied as a fractional physical supply bias normalized by the air-sea flux term in the GOP budget, where

$$\text{Physical supply}_{\text{fractional}} = \frac{\text{Physical supply}_{\text{model}}}{\text{Air-sea flux}_{\text{model}}} \times \text{Air-sea flux}_{\text{observations}} \qquad (6)$$

The sensitivity of the physical supply corrections to the magnitude of GOP in the model was tested by running a second simulation in which GOP was increased (1.7 times) while net primary production and all other model biogeochemistry remained unchanged. The 1.7× GOP simulation produced nearly identical fractional physical supply terms, which indicates that modeled fractional corrections are not sensitive to the magnitude of GOP and supports the use of model-based physical supply terms in the GOP budget.

2.3.3.2. Physical Supply Term in the NCP Budget

The physical supply contribution to the NCP budget was calculated using climatological data-based box models corresponding to the month and location of each discrete sample, similar to the approach previously described by *Lockwood* [2013]. Oxygen and argon physical supply tendency terms in equation (4) are calculated following

$$
\begin{cases}
z_{ml}\dfrac{\partial O_2}{\partial t}\bigg|_{phys} = \nabla\!\cdot\!\mathbf{u}_{Ek}O_2 + \nabla\!\cdot\!\mathbf{u}_{Geo}O_2 + \nabla\!\cdot\!\mathbf{w}_{Ek}\left(O_{2,ml} - O_{2,therm}\right)\\[2mm]
\qquad + \dfrac{\partial z_{ml}}{\partial t}\left(O_{2,ml} - O_{2,therm}\right) + K_z\left(\dfrac{O_{2,ml} - O_{2,therm}}{z_{ml} - z_{therm}}\right)\\[3mm]
z_{ml}\dfrac{\partial Ar}{\partial t}\bigg|_{phys} = \nabla\!\cdot\!\mathbf{u}_{Ek}Ar + \nabla\!\cdot\!\mathbf{u}_{Geo}Ar + \nabla\!\cdot\!\mathbf{w}_{Ek}\left(Ar_{ml} - Ar_{therm}\right)\\[2mm]
\qquad + \dfrac{\partial z_{ml}}{\partial t}\left(Ar_{ml} - Ar_{therm}\right) + K_z\left(\dfrac{Ar_{ml} - Ar_{therm}}{z_{ml} - z_{therm}}\right)
\end{cases}
\tag{7}
$$

where the RHS terms account for horizontal convergence due to Ekman transport ($\mathbf{u}_{Ek}$), horizontal convergence due to geostrophic transport ($\mathbf{u}_{Geo}$), upwelling due to Ekman-driven mass divergence ($\mathbf{w}_{Ek}$), entrainment of thermocline water due to mixed layer deepening (dz_{ml}/dt), and diffusive vertical mixing across the base of the mixed layer (K_z), respectively.

Data sources for all terms in equation (7) are given in Table 1. Since World Ocean Atlas (WOA) data includes oxygen but not argon, we assume that argon is at saturation, which accounts for the temperature dependence of gas solubility but not for effects of injection or cooling/heating-induced disequilibria. Previous work at OSP has found negligible changes in argon saturation across the mixed layer-thermocline boundary, suggesting that the differing effects of these processes across the thermocline boundary are minimal [*Giesbrecht et al.*, 2012].

The most poorly constrained parameter in physical supply terms is diffusive vertical mixing at the base of the mixed layer (K_z), since literature values for K_z vary by orders of magnitude (10^{-6} to 10^{-2} [*Demnan and Gargett*, 1983; *Brainerd and Gregg*, 1993; *Cronin et al.*, 2013, 2015]). To estimate a K_z value appropriate for the regions sampled in this study, we determine winter K_z in the Kuroshio and Western regions by assuming winter NCP ≈ 0 [*Emerson and Stump*, 2010] and solving for K_z following equations (4) and (7), yielding values of 5.1×10^{-4} and $3.6\times10^{-5}\,\mathrm{m^2\,s^{-1}}$, respectively. Observed winter O_2/Ar supersaturation in the Eastern region indicates net autotrophy even if K_z is reduced to 0, so we chose a low winter K_z of $2.0\times10^{-5}\,\mathrm{m^2\,s^{-1}}$. Winter K_z values were also applied in spring and were scaled down for summer and fall for each region based on seasonal cycle of K_z observed at the Kuroshio Extension Observatory (KEO, 32.4°N, 144.6°E) and OSP [*Cronin et al.*, 2015]. Reasonable variations in the winter NCP assumption and resulting choice of K_z do not significantly change key findings of this study (Table S1).

2.4. Calculation of Annual GOP and NCP Rates

The GOP and NCP rates determined from equations (2) and (4), respectively, determine productivity within and export from the seasonally varying mixed layer and thus are more appropriate for estimating seasonal than annual productivity rates. We present separate approaches for calculating annual rates of GOP and NCP, integrating to the base of the euphotic zone for GOP and to the deepest depth ventilated to the atmosphere during winter mixing (defined as the winter ventilation depth) for NCP.

GOP rates determined from equation (2) exclude sub-mixed layer production since it applies only within the seasonal mixed layer. Previous observational and modeling analyses at Station ALOHA in the subtropical North Pacific have shown that the annual integral of the air-sea TOI flux term closely (within 3%) approximates annual GOP (AGOP) integrated to the base of the euphotic zone [*Quay et al.*, 2010; *Nicholson et al.*, 2012]. CESM output further indicates that the annual integral of air-sea TOI flux approximates euphotic layer AGOP to within 6% across our sampling region in the North Pacific (Figure S1) and accounts for the fraction of AGOP occurring below the seasonal mixed layer (about one third). We therefore present euphotic zone AGOP as the annual integral of seasonal air-sea TOI flux.

As the mixed layer depth varies throughout the seasonal cycle, the effective depth to which NCP is integrated following the budget in equation (4) varies accordingly. Integrating seasonal NCP with time to determine annual NCP (ANCP) would yield overestimates because some of the organic carbon exported from the

shallow summertime mixed layer is subsequently respired before sinking out of the deeper mixed layer ventilated to the atmosphere during the following winter, as shown by *Körtzinger et al.* [2008]. To estimate an ANCP rate that represents carbon sequestered from the upper ocean over the annual cycle, one needs to integrate to the winter ventilation depth (which is slightly deeper than the winter mixed layer depth due to diffusive vertical mixing).

Long-term ANCP estimated to the winter ventilation depth has been determined previously in the North Atlantic by integrating air-sea oxygen flux over several annual cycles [*Quay et al.*, 2012]. This approach assumed no net O_2 transport out of the region. We build on this approach by accounting for O_2 transport out of the region from horizontal advection both within and below the mixed layer and upwelling across the base of the seasonal mixed layer.

$$\text{ANCP} = k[O_2]_{eq}\Delta O_2/\text{Ar} - z_{ml}\left(\frac{\partial O_2}{\partial t}_{\text{Geo+Ek}} - (O_2/\text{Ar})_{eq}\frac{\partial \text{Ar}}{\partial t}_{\text{Geo+Ek}}\right) - \tag{8}$$

$$\int_{z_{ml,max}}^{z_{ml}}\left(\frac{\partial O_2}{\partial t}_{\text{phys, sub-ml}} - (O_2/\text{Ar})_{eq}\frac{\partial \text{Ar}}{\partial t}_{\text{phys, sub-ml}}\right)dz$$

The RHS terms represent air-sea biological oxygen flux, physical supply due to horizontal advection of the mixed layer, and physical supply due to sub-mixed layer physical transport. Each RHS term is integrated over the full annual cycle, using seasonal mean data for each region.

Physical supply due to horizontal advection of the mixed layer (second RHS term in equation (8)) is calculated from the geostrophic and Ekman O_2 and Ar supply terms in equation (7). Sub-mixed layer physical supply of O_2 and Ar (third RHS term in equation (8)) are calculated from data sources in Table 1 following

$$\begin{cases} \dfrac{\partial O_2}{\partial t}_{\text{phys, sub-ml}} = \nabla\cdot\mathbf{u}_{Ek,z}O_2 + \nabla\cdot\mathbf{u}_{Geo,\ z}O_2 + \nabla\cdot\mathbf{w}_{Ek}\left(O_{2,z} - O_{2,z+\Delta z}\right) \\ \dfrac{\partial \text{Ar}}{\partial t}_{\text{phys, sub-ml}} = \nabla\cdot\mathbf{u}_{Ek,z}\text{Ar} + \nabla\cdot\mathbf{u}_{Geo,\ z}\text{Ar} + \nabla\cdot\mathbf{w}_{Ek}\left(\text{Ar}_z - \text{Ar}_{z+\Delta z}\right) \end{cases} \tag{9}$$

where the RHS terms account for horizontal convergence due to Ekman transport, horizontal convergence due to geostrophic transport, and vertical convergence due to upwelling, each for a particular depth between the base of the seasonal mixed layer (z_{ml}) and the maximum annual mixed layer depth ($z_{ml,max}$). Sub-mixed layer Ekman transport velocities were assumed equal to mixed layer transport velocity above the Ekman depth and 0 below the Ekman depth. Sub-mixed layer geostrophic velocities were calculated from relative geostrophic velocities at each depth interval based on geopotential anomalies calculated from WOA T and S, normalized to mixed layer geostrophic velocities. Upwelling rates driven by Ekman divergence were assumed constant throughout the sub-mixed layer region above $z_{ml,max}$.

2.5. Uncertainty Analysis

We quantify uncertainty in the seasonal and annual mean GOP and NCP estimates for each region resulting from two sources: (1) error in the method used to calculate GOP and NCP and (2) undersampling bias. Variability around the mean, reflecting spatial and temporal variability within each region, is reported as the standard deviation of the mean value.

Combined uncertainty from individual sources of error was determined using a Monte Carlo approach. Uncertainty in seasonal mean $^{17}\Delta$ and $\Delta O_2/\text{Ar}$ (2σ) was determined based on 3000 simulations where individual measured values varied according to sample-specific TOI and O_2/Ar measurement error. Additional uncertainty from estimation of the air-sea gas transfer rate (described in section 2.4) and the time rate of change and physical supply correction terms was included in the Monte Carlo simulations to estimate total methodological uncertainty, with these sources of uncertainty dominating over measurement error except where $\Delta O_2/\text{Ar}$ approaches 0. Uncertainty in estimating physical supply budget terms from modeled and climatological data products is difficult to quantify; however, as a representative estimate, we assume 50% uncertainty in all correction terms. Thus, when the magnitude of the correction terms in the GOP and NCP budgets is large, we estimate increased uncertainty in the calculated GOP and NCP rates. Vertical supply dominates the contribution of the correction terms to methodological uncertainty, with the time rate of change, horizontal supply, and upwelling terms playing a minor role.
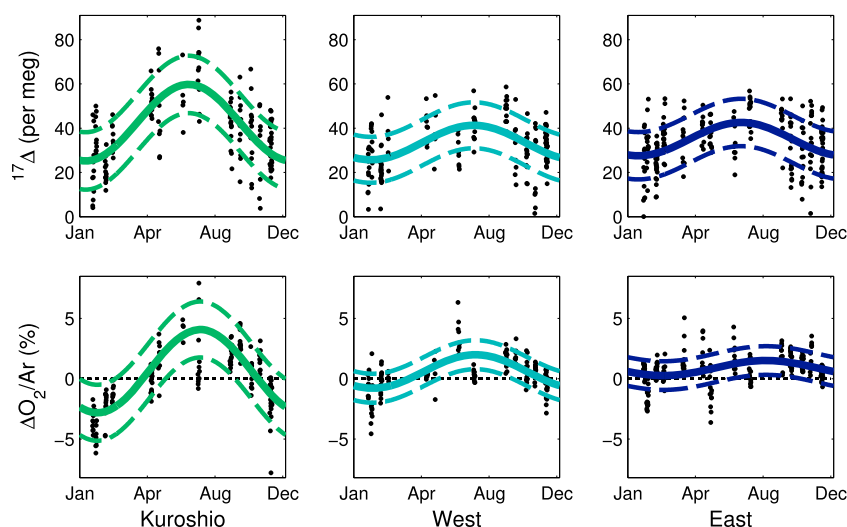
Figure 3. Composite annual cycle of $^{17}\Delta$ and $\Delta O_2/Ar$ in each region. Black dots show all discrete sample measurements in a given region (four samples with measured $^{17}\Delta < 0$ and four samples with measured $\Delta O_2/Ar > 9\%$ are outside the y axis bounds). The solid line is a harmonic fit to the data describing the annual cycle, and the dashed lines show the harmonic fit ± root-mean-square error.

We estimate the magnitude of undersampling bias in the air-sea flux terms as the percent difference between mean satellite-based chlorophyll concentrations calculated over the entire region and season versus those calculated using only the times and locations of our discrete sample collection (section 2.2; Figure 2). Potential undersampling could result from insufficient sampling of spatial variability throughout each region or from temporal gaps (for instance, a gap in spring sampling between early March and May in the Kuroshio and Western regions). While this is an imperfect metric because variability in chlorophyll may not match variability in productivity, it enables us to quantify the limitations of our sampling strategy. Methodological uncertainty and undersampling bias are combined to calculate total uncertainty in the air-sea flux terms for GOP and NCP. Methodological uncertainty dominates over undersampling bias in all regions and seasons except the Kuroshio in fall and the Western region in spring, where subsampled chlorophyll deviates most significantly from fully sampled regional mean chlorophyll (Figure 2). For annual rates, methodological uncertainty dominates in the Western and Eastern regions, but undersampling bias dominates (75–85% of total uncertainty) in the Kuroshio region.

3. Results and Discussion

3.1. Annual Cycle of TOI and O_2/Ar Observations

In each of the three regions, both $^{17}\Delta$ and O_2/Ar describe a seasonal cycle with a winter minimum and summer maximum (Figure 3 and Table 2). These tracer patterns reflect the combined influences of productivity, gas exchange, and physical supply. In summer, when the influence of physical supply is low and reduced wind speeds produce low gas transfer rates, GOP and NCP exert relatively strong influence to elevate mixed layer $^{17}\Delta$ and O_2/Ar. In winter, by contrast, entrainment and vertical mixing exert a strong influence on mixed layer $^{17}\Delta$ and O_2/Ar, evident in particular in significant winter O_2/Ar undersaturation in the Kuroshio and Western regions.

The amplitude of the seasonal cycle for both $^{17}\Delta$ and O_2/Ar is largest in the Kuroshio and decreases eastward across the basin. Spatial and temporal variability, as reflected in the standard deviations of the mean tracer values, are also highest in the Kuroshio and decrease eastward (Table 2). This is consistent with more complex physical dynamics and stronger mesoscale eddy activity in the region influenced by the Kuroshio, Oyashio, and Kuroshio Extension currents, which would be expected to increase spatial and temporal heterogeneity in biological productivity [Sasai et al., 2010].

3.2. Seasonal GOP and NCP Budgets

The seasonal cycle of GOP and NCP calculated from the tracer budgets in equations (2) and (4) are shown in Figure 4 and Table 2. Regional means and associated uncertainty values for each budget term in each season

Table 2. Summary of Regional Mean Geochemical Tracer Values and Productivity Rates Across the North Pacific[a]

	No. of Samples	$^{17}\Delta$ (per meg)	ΔO_2/Ar (% Supersaturation)	GOP		NCP		NCP/GOP
				Mixed Layer	Euphotic Zone	Mixed Layer	Full Depth	
Kuroshio (142°E–170°E)								
Spring (MAM)	26	50 ± 2 (12)	1.38 ± 0.09 (3.9)	238 ± 57	274 ± 65	27 ± 7	30 ± 7	0.11 ± 0.04
Summer (JJA)	17	63 ± 3 (15)	3.10 ± 0.12 (3.5)	108 ± 33	167 ± 51	16 ± 2	23 ± 3	0.15 ± 0.05
Fall (SON)	51	38 ± 2 (16)	1.87 ± 0.04 (1.8)	120 ± 120	161 ± 161	20 ± 12	25 ± 15	0.17 ± 0.19
Winter (DJF)	73	29 ± 1 (12)	−2.38 ± 0.04 (1.7)	201 ± 45	205 ± 46	0 ± 19	0 ± 19	--
Annual	169	--	--	60 ± 22	74 ± 20	5.8 ± 2.2	0.7 ± 1.0	0.01 ± 0.02
West (170°E 160°W)								
Spring (MAM)	20	37 ± 3 (10)	0.31 ± 0.10 (0.8)	197 ± 62	227 ± 72	21 ± 4	23 ± 5	0.11 ± 0.04
Summer (JJA)	21	37 ± 3 (9)	1.68 ± 0.10 (1.9)	93 ± 24	144 ± 37	15 ± 3	21 ± 4	0.16 ± 0.05
Fall (SON)	50	34 ± 2 (14)	1.17 ± 0.04 (0.9)	118 ± 44	158 ± 59	15 ± 3	19 ± 4	0.13 ± 0.05
Winter (DJF)	74	27 ± 1 (10)	−0.66 ± 0.04 (1.2)	137 ± 38	141 ± 39	0 ± 7	0 ± 7	--
Annual	166	--	--	49 ± 13	63 ± 12	4.7 ± 1.0	2.7 ± 0.8	0.04 ± 0.01
East (160°W–125°W)								
Spring (MAM)	61	36 ± 2 (9)	0.64 ± 0.06 (1.5)	167 ± 23	192 ± 27	13 ± 2	14 ± 3	0.08 ± 0.02
Summer (JJA)	25	42 ± 2 (10)	1.07 ± 0.09 (1.2)	58 ± 22	90 ± 34	5 ± 1	7 ± 1	0.09 ± 0.04
Fall (SON)	68	34 ± 2 (13)	1.59 ± 0.04 (0.8)	92 ± 40	123 ± 54	19 ± 3	24 ± 4	0.20 ± 0.09
Winter (DJF)	92	27 ± 1 (11)	0.20 ± 0.03 (1.0)	102 ± 25	104 ± 25	4 ± 2	4 ± 2	--
Annual	246	--	--	38 ± 10	50 ± 7	3.7 ± 0.6	3.3 ± 0.5	0.07 ± 0.01

[a]All results are given as mean ± uncertainty, reflecting both methodological error and sampling bias (see text for details). For tracer values, 1σ variability about the mean is given in parentheses, reflecting regional variability. GOP and NCP are reported in mmol O_2 m^{-2} d^{-1} for seasonal rates and mol O_2 m^{-2} yr^{-1} for annual rates. NCP/GOP is unitless. Seasonal euphotic zone GOP and full (i.e. compensation) depth NCP include sub-mixed layer production as estimated from CESM output (see Figure S2). Euphotic zone AGOP rates are the annually integrated air-sea TOI flux, and full depth ANCP rates are integrated to the winter ventilation depth following equation (8). Seasonal NCP/GOP is calculated from mixed layer productivity rates, and annual NCP/GOP is calculated from euphotic zone AGOP and winter ventilation depth ANCP.

are in Tables S2 (GOP) and S3 (NCP). The seasonal cycle is similar in all regions, with a pronounced spring bloom in GOP and elevated spring NCP. GOP in all seasons and NCP in spring and summer are highest in the Kuroshio and decrease in magnitude eastward across the basin.

3.2.1. Influence of Physical Supply on Seasonal Budgets

The magnitude of the physical supply and nonsteady state terms illustrate deviation from the assumption that air-sea tracer flux alone represents GOP and NCP. Vertical supply from diffusive mixing and entrainment dominate these terms in the seasonal GOP and NCP budgets, with upwelling, horizontal advection, and nonsteady state processes playing a minor role (Figure 4). Variations in the influence of vertical supply over the year reflect the seasonal cycle in both the strength of entrainment and vertical diffusion and the gradients in TOI and O_2/Ar across the base of the mixed layer.

For GOP, the influence of vertical supply is strongest in fall when mixed layer deepening entrains the elevated $^{17}\Delta$ signature from summer photosynthesis in the sub-mixed layer portion of the euphotic zone. During summer, vertical supply is driven by strong TOI gradients despite relatively low vertical exchange across the strongly stratified summer mixed layer, while during winter, vertical supply is driven by strong vertical mixing and entrainment as the mixed layer deepens but relatively weaker TOI gradients once the entire summer euphotic zone has been ventilated. The minimum influence of vertical supply on the GOP budget is in spring, when the vertical TOI gradient is reduced following winter mixing and there is no influence of entrainment as the mixed layer shoals. The seasonal cycle in the GOP vertical supply term is fairly similar across the entire basin (Figure 4 and Table S2).

The seasonal pattern of physical supply influence on the NCP budget differs significantly from that for the GOP budget, with the vertical supply term for NCP playing the largest role in winter and spring. The vertical gradient in O_2/Ar across the base of the mixed layer is greatest in winter and spring when respiration produces strong oxygen undersaturations in the thermocline. For GOP, in contrast, TOI is not influenced by respiration and the vertical gradient is strongest in late summer and fall. The magnitude of the seasonal cycle in the NCP physical supply terms decreases dramatically eastward across the basin, driven by winter physical supply that offsets large negative air-sea flux in the Kuroshio region but approaches 0 in the Eastern region. This effect is dominated by deeper winter mixed layers and stronger winter mixing in the western basin, yielding larger entrainment and vertical diffusion terms.
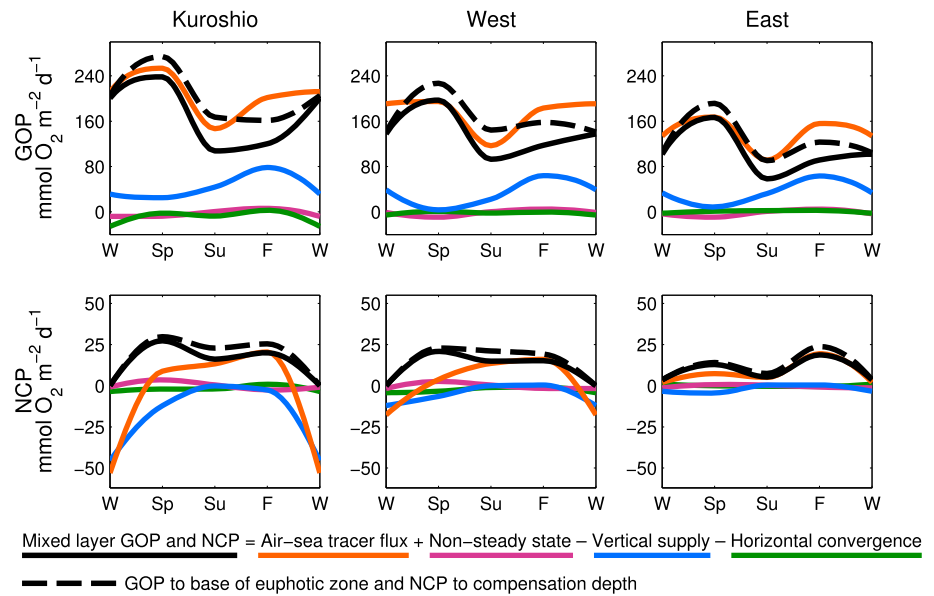
Figure 4. Seasonal cycle of (top) GOP and (bottom) NCP in each region, including component budget terms, calculated following equations (2) and (4), respectively. Vertical supply includes both entrainment and vertical diffusion. Horizontal convergence includes both Ekman and geostrophic transport. Upwelling is a minor contribution to the budget and is omitted for clarity. Seasonal GOP to the base of the euphotic zone and NCP to the compensation depth (where photosynthesis = respiration) include sub-mixed layer production estimated from CESM output (Figure S2). For all budget terms including uncertainty values, see Tables S2 and S3.

3.2.2. Influence of Mixed Layer Depth on the Seasonal GOP and NCP Cycles

Since the GOP and NCP budgets integrate to the base of the seasonal mixed layer, they are affected by seasonal changes in mixed layer depth. During the period when the mixed layer is shallower than the euphotic zone in late spring through early fall, photosynthesis occurs below the mixed layer, contributing additional GOP and NCP not included in the mixed layer budgets. To estimate the fraction of the total GOP and NCP occurring below the mixed layer, we use depth-resolved photosynthesis and respiration output from CESM in the North Pacific (Figure S2). We apply a single basin-wide estimate of sub-mixed layer production rather than a spatially varying estimate to avoid introducing spatial biases in CESM productivity in our tracer-based estimates and because the resulting seasonal cycle estimates are largely insensitive to this choice. During summer (June–August) when the mixed layers are shallowest (~20 m), 55% of the total euphotic zone GOP and 42% of the total NCP to the compensation depth occurs below the mixed layer.

We estimate seasonal GOP and NCP rates including sub-mixed layer production by scaling up the tracer-based mixed layer rates using CESM estimates of the fraction of GOP and NCP occurring below the mixed layer in each season (Figure 4). Across the basin, GOP shows maximum rates in spring, which decrease during summer and then slightly increase during fall. A similar seasonal trend is seen in MODIS chlorophyll concentrations for all regions (Figure 2), suggesting that the observed seasonal cycle in GOP may reflect seasonal migration of the TZCF across these regions (Figure S3). When the TZCF is at its northernmost location in summer (~40°N), a larger proportion of each region is within the less productive lower chlorophyll area south of the front, which reduces GOP. Then in fall as the TZCF migrates south there is a corresponding GOP increase. During winter, when the TZCF is at its farthest south location, GOP matches or exceeds summer rates in all regions. Winter GOP is further discussed in section 3.2.4.

The seasonal cycle for NCP is similar to that for GOP, with spring and fall NCP rates greater than or comparable to summer rates in all regions, but with a less pronounced spring maximum in the Kuroshio and West for NCP than for GOP and the annual maximum NCP in the East occurring in fall rather than spring. This indicates seasonal changes in export efficiency, with a greater fraction of GOP contributing to export in fall than in spring, consistent with previous estimates in the eastern North Pacific [*Juranek et al.*, 2012]. Winter NCP was assumed to approach 0 in all regions (see section 2.3.3.2), precluding the ability to interpret this portion of the seasonal cycle.

3.2.3. Comparison With Previous Seasonal Productivity Estimates

North Pacific primary and export production north of the subtropics have previously been measured in most detail at two time series locations: OSP just north of our Eastern region and KNOT in the Kuroshio region, both representing the subarctic gyres [e.g., *Harrison et al.*, 1999, 2004]. Primary productivity has primarily been described based on ^{14}C incubation-based net primary production (NPP), with the only previous GOP estimates (based on TOI) from spring and early fall transects across the Eastern region [*Juranek et al.*, 2012]. We convert our GOP rates to ^{14}C-NPP equivalent rates to compare to previous measurements using an empirically determined gross O_2:net C ratio of 2.7 [*Marra*, 2002]. Export production has been previously estimated based on nutrient, oxygen, and carbon mass balance, ^{234}Th-^{238}U disequilibrium, and $^{15}NO_3^-$ incubation experiments. We convert our NCP rates from oxygen to carbon units to compare to previous measurements using a O_2:C ratio of 1.4 [*Laws*, 1991].

In the Eastern region, our estimates of NPP and NCP are generally comparable to previous measurements at OSP and in the broader region over the spring through fall productive season (Tables 3 and 4). The greatest discrepancy is in summer, when our estimates of mean NPP and NCP are about half of previous measurements even when sub-mixed layer production is included, likely reflecting lower productivity south of the TZCF in the region covered by our cruise tracks while OSP remains north of the TZCF year-round. In the Kuroshio region, by contrast, our estimates of NPP are about double previous measurements at KNOT during spring-fall and an order of magnitude higher in winter (Table 3). For NCP our estimates are 1–2 times higher than previous measurements in spring–fall, though generally agree within uncertainty (Table 4). Given the high spatial variability in the TOI, O_2/Ar, SST, and chlorophyll observations in the Kuroshio region, it is not surprising that there is greater discrepancy between results and this suggests that measurements primarily at a single time series station in the western subarctic gyre do not reflect productivity trends throughout the broader region. In contrast, OSP appears to more fully reflect productivity throughout the less dynamic Eastern region. These observations are consistent with recent model analyses of time series observing stations' spatial footprints showing that OSP represents more than twice the area of western subarctic gyre station K2 (near KNOT, at 47°N, 160°E) for both primary production and export [*Henson et al.*, 2016].

3.2.4. Winter GOP in the Kuroshio Region

Because of the large (15 times) discrepancy between our estimate of wintertime NPP in the Kuroshio region compared to previous results, we further verify winter GOP rates by analyzing depth profiles of TOI and O_2/Ar from four locations in the Kuroshio region collected during a research cruise in February–March 2013 (Figure S4). The depth profile observations more tightly constrain TOI and O_2/Ar budgets and, therefore, estimated winter GOP and NCP rates because we avoid using the CESM- and WOA-based physical supply corrections.

Given that vertical supply and air-sea flux are the major terms in the GOP and NCP budgets, we estimate GOP and NCP from these profiles assuming negligible time rate of change and horizontal supply:

$$\text{GOP} \approx \frac{k[O_2]_{eq}\left(^{17}\Delta_{ml} - {}^{17}\Delta_{eq}\right)}{\left(^{17}\Delta_P - {}^{17}\Delta_{ml}\right)} - \frac{T_{vert}\left([O_2]_{therm}{}^{17}\Delta_{therm} - [O_2]_{ml}{}^{17}\Delta_{ml}\right)}{\left(^{17}\Delta_P - {}^{17}\Delta_{ml}\right)} \quad (10)$$

$$\text{NCP} = k[O_2]_{eq}\Delta O_2/\text{Ar} - T_{vert}\left(\left(O_{2,ml} - O_{2,therm}\right) - (O_2/\text{Ar})_{eq}(\text{Ar}_{ml} - \text{Ar}_{therm})\right) \quad (11)$$

where the first RHS terms are air-sea tracer flux as defined in equations (2) and (4), and in the second RHS terms, T_{vert} represents the total vertical transport by entrainment, vertical diffusion, and upwelling across the base of the mixed layer (m d^{-1}). The subscripts "P," "therm," and "ml" represent the photosynthetic end-member, thermocline, and mixed layer, respectively. All terms in equation (10) are expressed here using $^{17}\Delta$ for simplicity but are calculated directly from $\delta^{17}O$ and $\delta^{18}O$ (see *Nicholson et al.* [2014, equation (S7)] for the full vertical supply equation). Oxygen and argon concentrations in equation (11) are calculated from measured O_2/Ar by assuming that argon is at saturation, as discussed previously.

Equations (10) and (11) provide two equations to constrain three unknown values: GOP, NCP, and T_{vert}. We therefore determine possible GOP and T_{vert} rates at each depth profile location over a range of possible NCP rates (Figure 5). Since ΔO_2/Ar decreases (becomes more undersaturated) and $^{17}\Delta$ increases with depth across the mixed layer-thermocline boundary (Figure S4), a decrease in prescribed NCP in equation (11) reduces estimated T_{vert} and increases GOP estimated in equation (10). Uncertainty in all terms is estimated using a Monte Carlo approach accounting for uncertainty in tracer measurements and the air-sea-gas transfer

Table 3. Net Primary Productivity (NPP) Estimates for the Kuroshio and Eastern Regions of the North Pacific[a]

	Annual	Spring	Summer	Fall	Winter
		Kuroshio			
KNOT	7.5[b]	44[b]	19[b], 23[c]	14[b], 44[c]	4[b]
Elsewhere	7.3[d]	65[b], 39[d], 29[c], 111[e]	19[d], 26[c], 35[f], 39[g]	16[d], 30[c], 31[h]	6[d]
Mean ± 1σ	7.4 ± 0.1	58 ± 33	27 ± 8	27 ± 12	5 ± 1
This study					
Mixed layer	22 ± 8	88 ± 21	40 ± 12	44 ± 44	74 ± 17
Euphotic zone	28 ± 7	102 ± 24	62 ± 19	60 ± 20	76 ± 17
		East			
OSP	14[i], 12[j], 18[k]	46[i], 35[j], 71[k]	73[i], 39[j], 71[k]	21[h], 62[i], 31[j]	24[j], 25[k]
Elsewhere		70[l], 74[l]	28[m]	26[l], 69[l]	
Mean ± 1σ	15 ± 3	59 ± 18	53 ± 23	42 ± 22	24 ± 1
This study					
Mixed layer	14 ± 4	62 ± 9	22 ± 8	34 ± 15	38 ± 9
Euphotic zone	19 ± 3	71 ± 10	33 ± 13	46 ± 20	39 ± 9

[a]Annual NPP in mol C m^{-2} yr^{-1}; seasonal NPP in mmol C m^{-2} d^{-1}. All previous measurements are ^{14}C or ^{13}C incubations, unless otherwise indicated. Sampling locations are noted for values from elsewhere than KNOT or OSP. We summarize previous measurements annually and seasonally in each region as the mean ± 1σ of all previous studies' mean values. GOP values from this study are converted to ^{14}C-NPP equivalent rates using a gross O_2:net C ratio of 2.7 [*Marra*, 2002].
[b]*Imai et al.* [2002]; values from KNOT as well as a May bloom near KNOT (44–45°N, 155.5–156.5°E).
[c]*Kawakami and Honda* [2007]; values from KNOT as well as stations K1 (51°N, 165°E), K2 (47°N, 160°E), and K3 (39°N, 160°E).
[d]*Shiomoto* [2000]; 40–45°N, 150–160°E.
[e]*Isada et al.* [2010]; 41–43°N, 144–147°E.
[f]*Fujiki et al.* [2011]; fast repetition rate fluorometry from profiling float at K2, calibrated with ^{13}C incubations.
[g]*Elskens et al.* [2008]; K2.
[h]*Kawakami et al.* [2010a]; Kuroshio region value from 47–51°N, 160–169°E, including K1 and K2.
[i]*Welschmeyer et al.* [1993].
[j]*Wong et al.* [1995].
[k]*Boyd and Harrison* [1999], as presented in *Harrison et al.* [1999].
[l]*Juranek et al.* [2012]; GOP from TOI, converted to NPP with a gross O_2:net C ratio of 2.7. Values from the subtropical-subarctic physical transition zone (31–43°N, 145–160°W) and the subarctic gyre (39–55°N, 145–160°W).
[m]*Giesbrecht et al.* [2012]; seasonal mean from OSP and station P16 (49.3°N, 134.7°W).

velocity. We expect wintertime NCP to approach 0 [*Emerson and Stump*, 2010]. Estimates of particulate organic carbon export from ^{234}Th yield slight net autotrophy at KNOT and OSP in winter (2–3 mmol C m^{-2} d^{-1} [*Charette et al.*, 1999; *Kawakami et al.*, 2004; *Kawakami and Honda*, 2007]), while recent oxygen and carbon annual budgets accounting for dissolved as well as particulate organic carbon at OSP have found wintertime net heterotrophy [*Bushinsky and Emerson*, 2015; *Fassbender et al.*, 2016]. We determine GOP rates for a wider range of NCP than is likely plausible, spanning −25 to 25 mmol O_2 m^{-2} d^{-1}, and find a mean GOP rate of 125 ± 52 mmol O_2 m^{-2} d^{-1} (Figure 5). These GOP rates are 38% lower than the Kuroshio region mixed layer winter GOP rate of 201 ± 45 mmol O_2 m^{-2} d^{-1} but when converted to net carbon units (i.e., GOP/2.7) yield an NPP rate of 46 ± 19 mmol C m^{-2} d^{-1} that substantially exceeds (by ~10 times) previous NPP estimates (5 ± 1 mmol C m^{-2} d^{-1}) in this region (Table 3). The results of this analysis support our conclusion that NPP rates during winter in the Kuroshio region are 10–15 times higher than rates measured previously by ^{14}C incubation at KNOT, which suggests that a single time series station is insufficient to accurately represent the region.

3.3. Annual Gross Oxygen Production (AGOP)

AGOP through the full euphotic zone, as determined from annually integrated air-sea TOI flux, and in the mixed layer, as determined by integrating equation (2) over the annual cycle, is highest in the Kuroshio region and decreases eastward across the basin, with sub-mixed layer production contributing 19–25% of the total euphotic zone GOP (Figure 6a and Tables 2 and S4). The observed trend is consistent with stronger nutrient supply from deeper winter mixing and greater aeolian iron supply from dust input in the western than the eastern basin [*Duce and Tindale*, 1991]. However, previous estimates of annual NPP at KNOT and OSP found the opposite trend, with ^{14}C-based annual NPP in the eastern subarctic at OSP estimated as about twice that at KNOT (Table 3). The difference in these results is primarily because our TOI-based annual NPP estimates are ~4 times previous ^{14}C-based estimates in the Kuroshio region but comparable to results at OSP in the Eastern region (Table 3).

Table 4. Net Community Productivity (NCP) Estimates for the Kuroshio and Eastern Regions of the North Pacific[a]

	Annual	Productive Season	Spring	Summer	Fall
		Kuroshio			
KNOT		4.5[b], 5.1[c]	5[d], 2.5[e]	12[e]	10[d], 10[e]
Elsewhere		3.2[f], 2.9[g], 3.3[c], 4.0[c], 4.8[h], 2.6[e], 1.9[e], 6.3[i], 2.7[i], 6.9[i], 4.2[j], 5.3[j], 4.5[k]	7[g], 19[d], 6[e]	24[g], 10[e], 8[l]	8[d], 5[e], 4[m]
Mean ± 1σ		4.1 ± 1.4	8 ± 6	13 ± 7	7 ± 3
This study					
Mixed layer		4.1 ± 1.6	19 ± 5	12 ± 2	14 ± 8
Full depth	0.5 ± 0.7		21 ± 5	16 ± 2	18 ± 10
		East			
OSP	0.7[n]	3.0[h], 2.2[o], 2.1[p], 1.6[p], 2.5[p], 2[k], 1.4[n]	35[q], 24[q]	8[r], 6[q], 21[q], 22[s], 15[p], 10[p], 17[p]	3[m], 19[q]
Elsewhere	2.2 (0.5–4)[t]	3.1[i], 1.8[j], 1.3[j]	7[r], 15[u], 2[u]	13[v], 7[v], 8[w]	3[w], 12[x], 26[x], 9[u], 22[u]
Mean ± 1σ	1.5 ± 1.1	2.1 ± 0.6	17 ± 13	13 ± 6	13 ± 9
This study					
Mixed layer		2.6 ± 0.4	9 ± 2	4 ± 1	13 ± 2
Full depth	2.3 ± 0.3		10 ± 2	5 ± 1	17 ± 3

[a]Annual and productive season NCP in mol C m^{-2} yr^{-1}; seasonal NCP in mmol C m^{-2} d^{-1}. Sampling locations are noted for values not from KNOT or OSP. We summarize previous measurements annually and seasonally in each region as the mean ± 1σ of all previous studies' mean values. NCP values from this study are converted to carbon units using a O$_2$:C ratio of 1.4 [*Laws*, 1991]. Full depth seasonal NCP includes sub-mixed layer production to the compensation depth, and full depth annual NCP is integrated to the winter ventilation depth.
[b]*Tsurushima et al.* [2002]; carbon and nitrate drawdown from top 100 m, May to October, 1998 and 1999.
[c]*Kawakami et al.* [2007]; carbon and nitrate drawdown from top 100 m, April to October. Values elsewhere than KNOT from stations K1 (51°N, 165°E) and K2 (47°N, 160°E).
[d]*Kawakami et al.* [2004]; particulate carbon flux to the base of the euphotic zone from ^{234}Th, 40–50°N, 150–170°E.
[e]*Kawakami and Honda* [2007]; particulate carbon flux to 100 m from ^{234}Th. Values elsewhere than KNOT from K1, K2, and K3 (39°N, 160°E). Annual values from K2 and K3.
[f]*Andreev et al.* [2002]; carbon and nitrate budget in top 100 m, includes data from KNOT and central western subarctic gyre (50°N, 165–170°E).
[g]*Midorikawa et al.* [2002, 2003]; seasonal carbon and nitrate drawdown, 48°N, 165°E.
[h]*Kawakami et al.* [2010b]; carbon and nitrate budget in top 100 m, K2 and OSP.
[i]*Wong et al.* [2002a]; carbon and nitrate mixed layer budget. Kuroshio regions are the western subarctic gyre (45–55°N, 140–160°E), southeast Japan (42–45°N, 140–160°E), and Hokkaido (35–42°N, 140–160°E); Eastern region is the Alaskan gyre (45–55°N, 140–170°W).
[j]*Chierici et al.* [2006]; carbon and nitrate mixed layer budget. Kuroshio regions are the Oyashio (41–47°N, 145–155°E) and western subarctic gyre (45–51°N, 155–165°E); Eastern regions are the Alaskan gyre (45–52°N, 150–165°W) and subarctic (47–51°N, 135–145°W).
[k]*Fassbender* [2014]; *Fassbender et al.* [2016]; carbon and alkalinity budgets at OSP and KEO (32.3°N, 144.6°E).
[l]*Elskens et al.* [2008]; ^{15}NO$_3$$^-$ uptake in top 50 m at K2.
[m]*Kawakami et al.* [2010a]; particulate carbon flux to 100 m from ^{234}Th. Kuroshio value from 47–51°N, 160–169°E, including K1 and K2.
[n]*Bushinsky and Emerson* [2015]; O$_2$ budget from profiling float.
[o]*Wong et al.* [2002b]; nitrate drawdown from top 50 m over 6 month productive season.
[p]*Emerson* [1987]; *Emerson et al.* [1991]; *Emerson and Stump* [2010]; O$_2$ and inert gas mixed layer budgets, assuming 150 day productive season from May to September.
[q]*Wheeler* [1993]; nitrate drawdown for spring (May) and summer (May–September); ^{15}NO$_3$$^-$ uptake for spring (May), summer (June and August), and fall (September), converted from nitrogen to carbon units with 16 N:106 C [*Redfield et al.*, 1963].
[r]*Charette et al.* [1999]; particulate carbon flux to the base of the euphotic zone from ^{234}Th. Spring value is mean along Line P in Alaskan gyre.
[s]*Varela and Harrison* [1999]; ^{15}NO$_3$$^-$ uptake from May to September.
[t]*Sonnerup et al.* [2013]; apparent oxygen utilization from transit time distributions, 35–50°N, 145–152°W.
[u]*Juranek et al.* [2012]; O$_2$/Ar mixed layer budget, converted to C units with an O$_2$:C ratio of 1.4. Values from the subtropical-subarctic physical transition zone (31–43°N, 145–160°W) and the subarctic gyre (39–55°N, 145–160°W).
[v]*Giesbrecht et al.* [2012]; mixed layer O$_2$/Ar budget and ^{15}NO$_3$$^-$ uptake, OSP and station P16 (49.3°N, 134.7°W).
[w]*Howard et al.* [2010]; O$_2$/Ar euphotic zone budget, 30–45°N, 145–152°W.
[x]*Lockwood et al.* [2012]; O$_2$/Ar mixed layer budget. Values from the subtropical-subarctic physical transition zone (32–45°N, 145–152°W) and the subarctic gyre (45–50°N, 145–152°W).

Potential explanations for the discrepancy between previous Kuroshio region estimates and our results include the following: (1) Measurements primarily at a single time series station at KNOT in the dynamic Kuroshio region do not capture the full spatial variability in the region. (2) Incubation-based NPP measurements used in previous studies may fail to capture episodic pulses of productivity, which are more easily observed using the TOI approach since the measurements are integrated over the ~2 week residence time of dissolved oxygen in the surface mixed layer. (3) The gross O$_2$:net C conversion factor varies spatially from the constant 2.7 factor assumed here (as discussed in *Juranek and Quay* [2013]). However, this can only explain a small portion of the discrepancy as the GOP/NPP ratio of 8–10 that would be required to reconcile our AGOP estimates with annual NPP previously estimated at KNOT is at the high end of the GOP/NPP range of 2–8 previously observed in the ocean [*Juranek and Quay*, 2013] and well above the ratio of 3 ± 1 found in nutrient-limited laboratory cultures [*Halsey and Jones*, 2015].
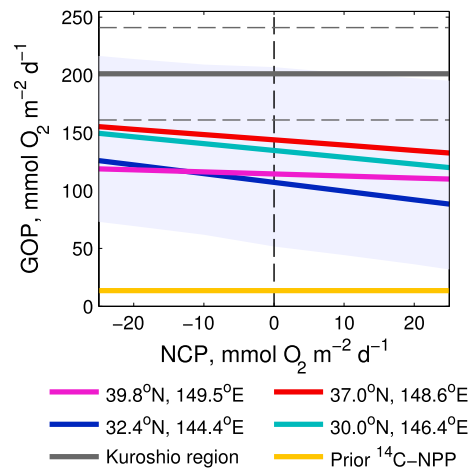
Figure 5. Winter GOP and NCP constrained by four depth profiles for TOI and O_2/Ar collected in late winter in the Kuroshio region (locations indicated in Figure 1; combined uncertainty bounds from all four depth profiles shaded in blue). Kuroshio region GOP from this study and previously measured ^{14}C-NPP in the region (from Table 3, converted to GOP using a gross O_2:net C ratio of 2.7) are plotted for comparison (uncertainty bounds shown with dashed lines, which are within the size of the line for prior ^{14}C-NPP). GOP and NCP are jointly constrained from depth profile data based on the assumption that the dominant budget terms are air-sea gas exchange and vertical supply (see text for details). Depth profile data are shown in Figure S4.

3.4. Annual Net Community Production (ANCP)

ANCP integrated to the winter ventilation depth, calculated separately from the seasonal NCP budget following equation (8), decreases westward across the North Pacific basin from 3.3 ± 0.5 and $2.7 \pm 0.7 \, mol \, O_2 \, m^{-2} \, yr^{-1}$ in the Eastern and Western regions, respectively, to $0.7 \pm 1.0 \, mol \, O_2 \, m^{-2} \, yr^{-1}$ in the Kuroshio region (colored bars in Figure 6b). These ANCP rates differ significantly from estimates of carbon export derived by considering only export from the seasonal mixed layer (black circles in Figure 6b), which show the opposite trend of export from the seasonal mixed layer instead increasing westward across the basin. By integrating NCP to the seasonal mixed layer depth rather than the winter ventilation depth, organic carbon (both particulate and dissolved) exported below the stratified seasonal mixed layer in spring through fall that is subsequently

respired in the seasonal thermocline and ventilated during winter mixing is "counted" as exported even though the carbon is not sequestered on annual or longer time scales. There is a strong gradient across the basin in the fraction of seasonally exported carbon that is respired and subsequently ventilated before sinking below the winter ventilation depth: 88% in the Kuroshio region, 42% in the Western region, and 12% in the Eastern region. The larger fraction of carbon respired in the seasonal thermocline in the western basin is likely driven largely by deeper winter mixing (Figure 1), which requires organic carbon to sink further through the water column to be effectively exported. In essence, although there is greater export of organic carbon from the seasonal mixed layer in the western than the eastern North Pacific, the deeper winter mixed layers in the west negate this trend and yield a lower export rate below the winter ventilation depth in the western than the eastern basin (Figure 6b).

Previous studies in midlatitude regions where winter mixing extends below the euphotic zone have demonstrated the significance of winter ventilation to annual carbon export. In the North Atlantic, ~40–45% of the carbon exported from the seasonally stratified mixed layer is remineralized above the winter mixed layer depth and ventilated during winter mixing [Körtzinger et al., 2008; Quay et al., 2012]. Recent studies at OSP
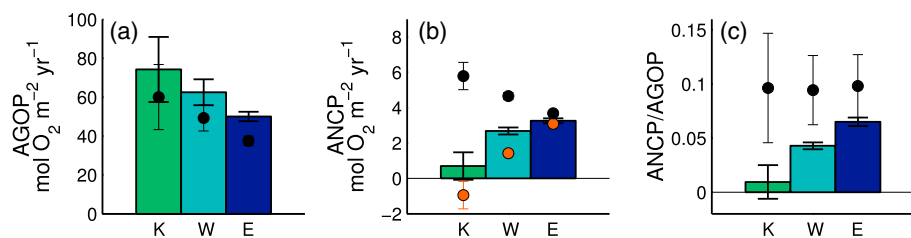

Figure 6. Colored bars are (a) AGOP to the base of the euphotic zone, calculated as the annual integral of air-sea flux of TOI, (b) ANCP to the winter ventilation depth, calculated following equation (8), and (c) annual export efficiency (ANCP/AGOP) in the Kuroshio (green), Western (light blue), and Eastern (dark blue) regions. Black circles are annual rates for each region determined to the base of the seasonal mixed layer (GOP calculated following equation (2) and NCP calculated following equation (4), as shown in Figure 4, each integrated over the year). Orange circles in Figure 6b are air-sea biological oxygen flux from O_2/Ar (as shown in Figure 4) integrated over the year in each region.

have similarly demonstrated the significance of winter processes to ANCP, with glider data showing accumulation of a sub-mixed layer respiration signature that is ventilated during winter mixing [*Pelland*, 2015] and float and mooring data showing ~30–50% of productive season NCP offset by winter respiration [*Bushinsky and Emerson*, 2015; *Fassbender et al.*, 2016]. CESM output for the North Pacific captures the phenomenon of mixing-driven ventilation across the basin, with a greater fraction of ANCP from the seasonal mixed layer respired above the maximum annual mixed layer and not contributing to ANCP at the winter mixed layer depth in areas with deeper winter mixed layers (Figures S5a and S5b). These results highlight the importance of including winter observations of seasonally exported carbon ventilated during winter mixing in estimating ANCP.

By measuring O_2/Ar throughout the full annual cycle, we were able to observe winter ventilation of O_2/Ar undersaturated waters in the Kuroshio and Western regions (Figure 3 and Table 2) and account for the reduced amount of carbon exported below the winter ventilation depth as compared to the seasonal mixed layer depth. If we assumed that net physical transport of O_2 via horizontal advection or upwelling were negligible, air-sea biological oxygen flux from these O_2/Ar measurements (first RHS term in equation (8); orange circles in Figure 6b; values given in Table S4) would approximate ANCP. However, physical transport of O_2 (second and third RHS terms in equation (8); rates for individual terms from equations (8) and (9) given in Table S4) plays a significant though secondary role contributing to winter O_2/Ar undersaturation in the western basin (contributions of -1.6 ± 1.0, -1.2 ± 1.1, and -0.2 ± 0.2 mol O_2 m^{-2} yr^{-1} in the Kuroshio, Western, and Eastern regions, respectively). The trend of a more negative physical transport term to the west is due to increased rates of Ekman-driven upwelling and eastward geostrophic advection by the Kuroshio Extension [*Jayne et al.*, 2009]. Thus, while a simpler budget including only air-sea biological oxygen flux effectively approximates ANCP in the Eastern region, it would underestimate ANCP in the more dynamic Kuroshio and Western regions. Future studies investigating ANCP to the winter ventilation depth and the role of remineralization of seasonally exported carbon should take care to account for the influence of physical transport, especially in similarly dynamic regions.

3.5. Export Efficiency

The NCP/GOP ratio provides a metric of the efficiency of the biological pump, defined as the fraction of photosynthetically fixed carbon that contributes to export. Efficiency of seasonal export from the surface mixed layer can be evaluated from mixed layer NCP/GOP, while annual export efficiency can be evaluated from ANCP/euphotic-depth AGOP to determine the fraction of total euphotic zone production that is exported past the winter ventilation depth. ANCP/AGOP (Figure 6c) is generally very low with the ratio decreasing westward across the basin from 0.07 ± 0.01 in the Eastern region to 0.01 ± 0.02 in the Kuroshio region. (The NPP/NCP ratio in carbon units would be about double the value in O_2 units, i.e., [GOP/2.7]/[NCP/1.4]). This spatial pattern opposes that of seasonal NCP/GOP in spring and summer and differs from annual NCP/GOP integrated to the base of the seasonal mixed layer, which is similar across the basin at 0.07–0.08 (Table 2, black circles in Figure 6c).

The basin-wide trend of lower seasonal export efficiency in spring and summer in the east than the west agrees with previous findings based on sediment trap, carbon, oxygen and nutrient budget, and ^{14}C-NPP estimates [*Honda*, 2003; *Harrison et al.*, 2004]. Elevated fall NCP/GOP in the Eastern region deviates from this trend of lower seasonal export efficiency in the east than the west but is consistent with the only previous NCP/GOP estimates in our study area (-0.01 to 0.13 in spring and 0.14 to 0.17 in fall in the Eastern region [*Juranek et al.*, 2012]), which agree with our observed NCP/GOP (0.08 ± 0.02 in spring and 0.20 ± 0.09 in fall). Seasonal NCP/GOP in all regions falls within the range previously observed from O_2 and TOI mass balance in other ocean regions (0.06 to 0.35, summarized by *Quay et al.* [2012]). The North Atlantic is the only region where annual export efficiency accounting for winter ventilation has previously been determined (ANCP/AGOP of 0.07 ± 0.06, *Quay et al.* [2012]). ANCP/AGOP in the Eastern region of the North Pacific matches that of the North Atlantic, while annual export efficiency in the Western and Kuroshio regions is lower than that in the North Atlantic or than seasonal export efficiency previously observed in other ocean regions.

Mechanistic explanations for variations in export efficiency have generally focused on the role of biological community composition. Larger phytoplankton cells sink faster than small cells and thus are more likely to sink out of the euphotic zone before being remineralized or grazed [*Smayda*, 1970], and ballasting by

biogenic silica or calcium carbonate increases sinking rates [*Armstrong et al.*, 2002; *Francois*, 2002; *Klaas and Archer*, 2002]. Based on this, we would expect higher export efficiency in the western than the eastern North Pacific, as the proportion of diatoms as compared to small cells in the phytoplankton community is greater in the west than the east [*Harrison et al.*, 2004]. This expected trend is consistent with our and previous studies' findings for seasonal export efficiency in spring and summer but the opposite of our observed trend in annual export efficiency, which is primarily the result of differences in the depth of winter ventilation across the basin. CESM output for the North Pacific similarly shows reduced annual export efficiency in regions where remineralization of seasonally exported organic material between the base of the stratified seasonal mixed layer and deep winter mixed layer reduces ANCP (Figure S5c). Our observations demonstrate that the physical dynamics of winter ventilation are a key parameter to be more fully considered in evaluating the efficiency of the biological pump on annual time scales.

4. Summary and Conclusions

The vessel of opportunity sampling approach employed in this study enabled the first basin-wide estimates of GOP and NCP rates across the North Pacific throughout the full annual cycle. Comparison with previous estimates shows that productivity east of 170°W is fairly well represented by time series measurements at OSP but that time series measurements at KNOT and other locations in the western subarctic underrepresent GOP and seasonal NCP in the more dynamic and spatially variable Kuroshio region west of 170°E. In particular, we observe significantly higher winter primary productivity in the Kuroshio region than previously measured. A more complete understanding of the rates and efficiency of carbon export in the western North Pacific and other highly dynamic regions across the globe will require sampling at higher spatial resolution than at single time series or mooring locations, using approaches such as vessel of opportunity sampling and autonomous measurements from bio-Argo floats [e.g., *Emerson and Bushinsky*, 2014].

The mixed layer budget approach used here to determine seasonal GOP and NCP from observed TOI and O_2/Ar demonstrates the importance of accounting for physical supply influence on tracer measurements applied over the full annual cycle. Especially in nonsummer months, strong vertical diffusion and entrainment and steep vertical tracer gradients exert significant influence on mixed layer TOI and O_2/Ar. Physical supply corrections are large for GOP in fall and winter and for NCP in winter and spring, with larger influence of physical supply in the more dynamic western basin. Improved constraints on gradients, particularly for TOI, can be achieved in future field programs by sampling the thermocline as well as the mixed layer as previously recommended by *Nicholson et al.* [2014], since the dominant physical supply is vertical. Improved constraints on rates of advection and mixing, particularly on diffusive vertical mixing, will also improve physical supply estimates.

Throughout the spring through fall productive season, GOP and NCP are highest in the Kuroshio region and decrease eastward across the basin. AGOP is also highest in the Kuroshio and decreases eastward, in contrast to previous estimates of annual primary production rates (Table 3 and Figure 6a). NCP from the seasonal mixed layer integrated over the spring through fall productive season also is highest in the Kuroshio and decreases eastward, with rates comparable to previous estimates (Table 4).

However, deep winter mixed layers (>200 m) in the Kuroshio and Western regions ventilate ~40–90% of the carbon exported from the seasonal mixed layer during the spring through fall productive season. Winter mixing does not penetrate as deeply in the Eastern region (<120 m) due to a strong permanent halocline [*Harrison et al.*, 1999], ventilating only ~10% of the seasonally exported carbon. As a result, annual NCP decreases westward across the basin from $2.3 \pm 0.3 \, mol \, C \, m^{-2} \, yr^{-1}$ east of 160°W to $0.5 \pm 0.7 \, mol \, C \, m^{-2} \, yr^{-1}$ west of 170°E, opposite the spatial trend of NCP from the seasonal mixed layer during the productive season. Our results demonstrate that annual estimates of carbon export to the deep ocean can only be resolved by accounting for winter ventilation of seasonally exported carbon in regions of deep winter mixing such as the western North Pacific. Estimates that only consider export below the shallow seasonal mixed layer during the highly stratified late spring–early fall months would tend to overestimate the contribution to annual carbon export. The ability of CESM to capture the influence of deeper winter mixing on ANCP in the North Pacific (Figure S5) indicates that global earth system model simulations could be used to investigate the role of winter ventilation on ANCP on the global scale, although additional observational estimates of ANCP to the winter ventilation depth are needed to validate modeled rates and spatial patterns of ANCP.

Annual export efficiency (ANCP/AGOP) increases eastward across the basin, with ANCP/AGOP in the Eastern region >6 times that in the Kuroshio (Figure 6c). This suggests that the larger phytoplankton blooms dominated by larger cells found in the western as compared to the eastern North Pacific [*Harrison et al.*, 2004], which likely produce the observed higher seasonal export efficiencies in the west than the east in spring and summer, play a less important role than physical constraints (i.e., winter ventilation depth) in controlling export efficiency on an annual basis. This could have significant implications in projecting how future climate change will influence the strength and efficiency of the biological pump. Increased stratification of the ocean is projected to both shift the phytoplankton community toward smaller cells and to decrease the depth of winter mixing. The shift to smaller cells is expected to decrease the efficiency of export, while the decreasing depth of winter mixing would increase the efficiency of annual export. Projections of future changes to biological carbon export should account for both of these competing influences.

References

Andreev, A., M. Kusakabe, M. Honda, A. Murata, and C. Saito (2002), Vertical fluxes of nutrients and carbon through the halocline in the western subarctic gyre calculated by mass balance, *Deep Sea Res., Part II*, 49, 5577–5593, doi:10.1016/S0967-0645(02)00200-X.

Armstrong, R. A., C. Lee, J. I. Hedges, S. Honjo, and S. G. Wakeham (2002), A new, mechanistic model for organic carbon fluxes in the ocean based on the quantitative association of POC with ballast minerals, *Deep Sea Res., Part II*, 49, 219–236.

Ayers, J. M., and M. S. Lozier (2012), Unraveling dynamical controls on the North Pacific carbon sink, *J. Geophys. Res.*, 117, C01017, doi:10.1029/2011JC007368.

Behrenfeld, M. J., and P. G. Falkowski (1997), Photosynthetic rates derived from satellite-based chlorophyll concentration, *Limnol. Oceanogr.*, 42(1), 1–20.

Bograd, S. J., D. G. Foley, F. B. Schwing, C. Wilson, R. M. Laurs, J. J. Polovina, E. A. Howell, and R. E. Brainard (2004), On the seasonal and interannual migrations of the transition zone chlorophyll front, *Geophys. Res. Lett.*, 31, L17204, doi:10.1029/2004GL020637.

Bopp, L., et al. (2013), Multiple stressors of ocean ecosystems in the 21st century: Projections with CMIP5 models, *Biogeosciences*, 10, 6225–6245, doi:10.5194/bg-10-6225-2013.

Boyd, P., and P. J. Harrison (1999), Phytoplankton dynamics in the NE subarctic Pacific, *Deep Sea Res., Part II*, 46, 2405–2432, doi:10.1016/S0967-0645(99)00069-7.

Brainerd, K. E., and M. C. Gregg (1993), Diurnal restratification and turbulence in the oceanic surface mixed layer: 1. Observations, *J. Geophys. Res.*, 98(C12), 22,645–22,656, doi:10.1029/93JC02298.

Bushinsky, S. M., and S. Emerson (2015), Marine biological production from in situ oxygen measurements on a profiling float in the subarctic Pacific Ocean, *Global Biogeochem. Cycles*, 29, doi:10.1002/2015GB005251.

Charette, M. A., S. B. Moran, and J. K. B. Bishop (1999), [234]Th as a tracer of particulate organic carbon export in the subarctic northeast Pacific Ocean, *Deep Sea Res., Part II*, 46, 2833–2861, doi:10.1016/S0967-0645(99)00085-5.

Chierici, M., A. Fransson, and Y. Nojiri (2006), Biogeochemical processes as drivers of surface fCO_2 in contrasting provinces in the subarctic North Pacific Ocean, *Global Biogeochem. Cycles*, 20, GB1009, doi:10.1029/2004GB002356.

Craig, H., and T. Hayward (1987), Oxygen supersaturation in the ocean: Biological versus physical contributions, *Science*, 235, 199–202.

Cronin, M. F., N. A. Bond, J. Thomas Farrar, H. Ichikawa, S. R. Jayne, Y. Kawai, M. Konda, B. Qiu, L. Rainville, and H. Tomita (2013), Formation and erosion of the seasonal thermocline in the Kuroshio Extension Recirculation Gyre, *Deep Sea Res., Part II*, 85, 62–74, doi:10.1016/j.dsr2.2012.07.018.

Cronin, M. F., N. A. Pelland, S. R. Emerson, and W. R. Crawford (2015), Estimating diffusivity from the mixed layer heat and salt balances in the North Pacific, *J. Geophys. Res. Oceans*, 120, 7346–7362, doi:10.1002/2015JC011010.

Demnan, K. L., and A. E. Gargett (1983), Time and space scales of vertical mixing and advection of phytoplankton in the upper ocean, *Limnol. Oceanogr.*, 28(5), 801–815, doi:10.4319/lo.1983.28.5.0801.

Duce, R. A., and N. W. Tindale (1991), Chemistry and biology of iron and other trace metals in the ocean, *Limnol. Oceanogr.*, 36(8), 1715–1726, doi:10.4319/lo.1991.36.8.1715.

Dunne, J. P., R. A. Armstrong, A. Gnanadesikan, and J. L. Sarmiento (2005), Empirical and mechanistic models for the particle export ratio, *Global Biogeochem. Cycles*, 19, 1–16, doi:10.1029/2004GB002390.

Elskens, M., N. Brion, K. Buesseler, B. A. S. Van Mooy, P. Boyd, F. Dehairs, N. Savoye, and W. Baeyens (2008), Primary, new and export production in the NW Pacific subarctic gyre during the vertigo K2 experiments, *Deep Sea Res., Part II*, 55, 1594–1604, doi:10.1016/j.dsr2.2008.04.013.

Emerson, S. (1987), Seasonal oxygen cycles and biological new production in surface waters of the subarctic Pacific Ocean, *J. Geophys. Res.*, 92(C6), 6535–6544.

Emerson, S., and S. Bushinsky (2014), Oxygen concentrations and biological fluxes in the open ocean, *Oceanography*, 27(1), 168–171, doi:10.5670/oceanog.2014.20.

Emerson, S., and C. Stump (2010), Net biological oxygen production in the ocean—II: Remote in situ measurements of O_2 and N_2 in subarctic pacific surface waters, *Deep Sea Res., Part I*, 57, 1255–1265, doi:10.1016/j.dsr.2010.06.001.

Emerson, S., P. Quay, C. Stump, D. Wilbur, and M. Knox (1991), O_2, Ar, N_2 and ^{222}Rn in surface waters of the subarctic ocean: Net biological O_2 production, *Global Biogeochem. Cycles*, 5(1), 49–69.

Emerson, S., C. Stump, D. Wilbur, and P. Quay (1999), Accurate measurement of oxygen, nitrogen and argon gases in water and the solubility of nitrogen, *Mar. Chem.*, 64, 337–347, doi:10.1016/S0304-4203(98)00090-5.

Fassbender, A. J. (2014), New approaches to study the marine carbon cycle, PhD thesis, Univ. of Washington, Seattle, Washington.

Fassbender, A. J., C. L. Sabine, and M. F. Cronin (2016), Net community production and calcification from seven years of NOAA Station Papa Mooring measurements, *Global Biogeochem. Cycles*, 30, doi:10.1002/2015GB005205, in press.

Francois, R. (2002), Factors controlling the flux of organic carbon to the bathypelagic zone of the ocean, *Global Biogeochem. Cycles*, 16(4), 1087, doi:10.1029/2001GB001722.

Fujiki, T., K. Matsumoto, S. Watanabe, T. Hosaka, and T. Saino (2011), Phytoplankton productivity in the western subarctic gyre of the North Pacific in early summer 2006, *J. Oceanogr.*, 67, 295–303, doi:10.1007/s10872-011-0028-1.

Garcia, H. E., and L. I. Gordon (1992), Oxygen solubility in seawater: Better fitting solubility equations, *Limnol. Oceanogr.*, *37*(6), 1307–1312.

Giesbrecht, K. E., R. C. Hamme, and S. R. Emerson (2012), Biological productivity along Line P in the subarctic northeast Pacific: In situ versus incubation-based methods, *Global Biogeochem. Cycles*, *26*, GB3028, doi:10.1029/2012GB004349.

Halsey, K. H., and B. M. Jones (2015), Phytoplankton strategies for photosynthetic energy allocation, *Annu. Rev. Mar. Sci.*, *7*, 265–297, doi:10.1146/annurev-marine-010814-015813.

Hamme, R. C. et al. (2012), Dissolved O2/Ar and other methods reveal rapid changes in productivity during a Lagrangian experiment in the Southern Ocean, *J. Geophys. Res.*, *117*, C00F12, doi:10.1029/2011JC007046.

Hamme, R., and S. Emerson (2004), The solubility of neon, nitrogen and argon in distilled water and seawater, *Deep Sea Res., Part I*, *51*(11), 1517–1528, doi:10.1016/j.dsr.2004.06.009.

Harrison, P. J., F. A. Whitney, A. Tsuda, H. Saito, and K. Tadokoro (2004), Nutrient and plankton dynamics in the NE and NW gyres of the subarctic Pacific Ocean, *J. Oceanogr.*, *60*, 93–117, doi:10.1023/B:JOCE.0000038321.57391.2a.

Harrison, P., P. Boyd, D. Varela, S. Takeda, A. Shiomoto, and T. Odate (1999), Comparison of factors controlling phytoplankton productivity in the NE and NW subarctic Pacific gyres, *Prog. Oceanogr.*, *43*(2-4), 205–234.

Henson, S. A., C. Beaulieu, and R. Lampitt (2016), Observing climate change trends in ocean biogeochemistry: When and where, *Global Change Biol.*, doi:10.1111/gcb.13152.

Honda, M. C. (2003), Biological pump in northwestern North Pacific, *J. Oceanogr.*, *59*, 671–684, doi:10.1023/B:JOCE.0000009596.57705.0c.

Howard, E., S. Emerson, S. Bushinsky, and C. Stump (2010), The role of net community production in air-sea carbon fluxes at the North Pacific subarctic-subtropical boundary region, *Limnol. Oceanogr.*, *55*(6), 2585–2596, doi:10.4319/lo.2010.55.6.2585.

Imai, K., Y. Nojiri, N. Tsurushima, and T. Saino (2002), Time series of seasonal variation of primary productivity at station KNOT (44°N, 155°E) in the sub-arctic western North Pacific, *Deep Sea Res., Part II*, *49*, 5395–5408.

Isada, T., A. Hattori-Saito, H. Saito, T. Ikeda, and K. Suzuki (2010), Primary productivity and its bio-optical modeling in the Oyashio region, NW Pacific during the spring bloom 2007, *Deep Sea Res., Part II*, *57*, 1653–1664, doi:10.1016/j.dsr2.2010.03.009.

Jayne, S. R., et al. (2009), The Kuroshio Extension and its recirculation gyres, *Deep Sea Res., Part I*, *56*, 2088–2099, doi:10.1016/j.dsr.2009.08.006.

Jonsson, B. F., S. C. Doney, J. Dunne, and M. Bender (2013), Evaluation of the Southern Ocean O2/Ar-based NCP estimates in a model framework, *J. Geophys. Res. Biogeosci.*, *118*, 385–399, doi:10.1002/jgrg.20032.

Juranek, L. W., and P. D. Quay (2005), In vitro and in situ gross primary and net community production in the North Pacific Subtropical Gyre using labeled and natural abundance isotopes of dissolved O_2, Global Biogeochem. Cycles, *19*, GB3009, doi:10.1029/2004GB002384.

Juranek, L., and P. Quay (2010), Basin-wide photosynthetic production rates in the subtropical and tropical Pacific Ocean determined from dissolved oxygen isotope ratio measurements, *Global Biogeochem. Cycles*, *24*, GB2006, doi:10.1029/2009GB003492.

Juranek, L. W., and P. D. Quay (2013), Using triple isotopes of dissolved oxygen to evaluate global marine productivity, *Annu. Rev. Mar. Sci.*, *5*, 503–24, doi:10.1146/annurev-marine-121211-172430.

Juranek, L. W., R. C. Hamme, J. Kaiser, R. Wanninkhof, and P. D. Quay (2010), Evidence of O_2 consumption in underway seawater lines: Implications for air-sea O_2 and CO_2 fluxes, *Geophys. Res. Lett.*, *37*, L01601, doi:10.1029/2009GL040423.

Juranek, L. W., P. D. Quay, R. A. Feely, D. Lockwood, D. M. Karl, and M. J. Church (2012), Biological production in the NE Pacific and its influence on air-sea CO_2 flux: Evidence from dissolved oxygen isotopes and O_2/Ar, *J. Geophys. Res.*, *117*, C05022, doi:10.1029/2011JC007450.

Kaiser, J. (2011), Technical note: Consistent calculation of aquatic gross production from oxygen triple isotope measurements, *Biogeosciences*, *8*, 1793–1811, doi:10.5194/bg-8-1793-2011.

Kawakami, H., and M. C. Honda (2007), Time-series observation of POC fluxes estimated from [234]Th in the northwestern North Pacific, *Deep Sea Res., Part I*, *54*, 1070–1090, doi:10.1016/j.dsr.2007.04.005.

Kawakami, H., Y. L. Yang, M. C. Honda, and M. Kusakabe (2004), Particulate organic carbon fluxes estimated from [234]Th deficiency in winters and springs in the northwestern North Pacific, *Geochem. J.*, *38*, 581–592.

Kawakami, H., M. C. Honda, M. Wakita, and S. Watanabe (2007), Time-series observation of dissolved inorganic carbon and nutrients in the northwestern North Pacific, *J. Oceanogr.*, *63*, 967–982, doi:10.1007/s10872-007-0081-y.

Kawakami, H., M. C. Honda, K. Matsumoto, T. Fujiki, and S. Watanabe (2010a), East–west distribution of POC fluxes estimated from [234]Th in the northern North Pacific in autumn, *Prog. Oceanogr.*, *66*, 71–83.

Kawakami, H., M. C. Honda, K. Matsumoto, T. Fujiki, and S. Watanabe (2010b), East-west distribution of nutrients and dissolved inorganic carbon in the northern North Pacific in autumn, *Open Ocean. J.*, *4*, 99–106.

Klaas, C., and D. E. Archer (2002), Association of sinking organic matter with various types of mineral ballast in the deep sea: Implications for the rain ratio, *Global Biogeochem. Cycles*, *16*(4), 1116, doi:10.1029/2001GB001765.

Körtzinger, A., U. Send, R. S. Lampitt, S. Hartman, D. W. R. Wallace, J. Karstensen, M. G. Villagarcia, O. Llinás, and M. D. DeGrandpre (2008), The seasonal pCO_2 cycle at 49°N/16.5°W in the northeastern Atlantic Ocean and what it tells us about biological productivity, *J. Geophys. Res.*, *113*, C04020, doi:10.1029/2007JC004347.

Lämmerzahl, P. (2002), Oxygen isotope composition of stratospheric carbon dioxide, *Geophys. Res. Lett.*, *29*(12), 1582, doi:10.1029/2001GL014343.

Laws, E. A. (1991), Photosynthetic quotients, new production and net community production in the open ocean, *Deep Sea Res.*, *38*(1), 143–167.

Laws, E., P. Falkowski, W. J. Smith, H. Ducklow, and J. McCarthy (2000), Temperature effects on export production in the open ocean, *Global Biogeochem. Cycles*, *14*(4), 1231–1246.

Liss, P. S., and L. Merlivat (1986), Air-sea gas exchange rates: Introduction and synthesis, in *The Role of Air-Sea Exchange in Geochemical Cycling*, edited by P. Buat-Menard, pp. 113–129, D. Reidel, Hingham, Mass.

Lockwood, D. E. (2013), Impact of the marine biological pump on atmospheric CO_2 uptake in the North Pacific: A study based on basin-wide underway measurements of oxygen/argon gas ratios and pCO_2, PhD thesis, Univ. of Washington, Seattle.

Lockwood, D., P. D. Quay, M. T. Kavanaugh, L. W. Juranek, and R. A. Feely (2012), High-resolution estimates of net community production and air-sea CO_2 flux in the northeast Pacific, *Global Biogeochem. Cycles*, *26*, GB4010, doi:10.1029/2012GB004380.

Luz, B., and E. Barkan (2000), Assessment of oceanic productivity with the triple-isotope composition of dissolved oxygen, *Science*, *288*, 2028–2031, doi:10.1126/science.288.5473.2028.

Luz, B., and E. Barkan (2005), The isotopic ratios $^{17}O/^{16}O$ and $^{18}O/^{16}O$ in molecular oxygen and their significance in biogeochemistry, *Geochim. Cosmochim. Acta*, *69*(5), 1099–1110, doi:10.1016/j.gca.2004.09.001.

Luz, B., and E. Barkan (2009), Net and gross oxygen production from O_2/Ar, $^{17}O/^{16}O$ and $^{18}O/^{16}O$ ratios, *Aquat. Microb. Ecol.*, *56*, 133–145, doi:10.3354/ame01296.

Marra, J. (2002), Approaches to the measurement of plankton production, in *Phytoplankton Productivity and Carbon Assimilation in Marine and Freshwater Ecosystems*, edited by P. J. Williams, D. R. Thomas, and C. S. Reynolds, pp. 78–108, Blackwell, London, doi:10.1002/9780470995204.ch4.

Midorikawa, T., T. Umeda, N. Hiraishi, K. Ogawa, K. Nemoto, N. Kubo, and M. Ishii (2002), Estimation of seasonal net community production and air-sea CO_2 flux based on the carbon budget above the temperature minimum layer in the western subarctic North Pacific, *Deep Sea Res., Part I*, *49*, 339–362, doi:10.1016/S0967-0637(01)00054-1.

Midorikawa, T., K. Ogawa, K. Nemoto, H. Kamiya, T. Umeda, N. Hiraishi, A. Wada, and M. Ishii (2003), Interannual variations of net community production and air-sea CO_2 flux from winter to spring in the western subarctic North Pacific, *Tellus*, *55B*, 466–477, doi:10.1034/j.1600-0889.2003.00009.x.

Monterey, G., and S. Levitus (1997), Seasonal variability of the mixed layer depth for the world ocean, *NOAA Atlas NESDIS*, *14*(5), 96.

Nicholson, D. P., R. H. R. Stanley, E. Barkan, D. M. Karl, B. Luz, P. D. Quay, and S. C. Doney (2012), Evaluating triple oxygen isotope estimates of gross primary production at the Hawaii Ocean Time-series and Bermuda Atlantic Time-series Study sites, *J. Geophys. Res.*, *117*, C05012, doi:10.1029/2010JC006856.

Nicholson, D., R. H. R. Stanley, and S. C. Doney (2014), The triple oxygen isotope tracer of primary productivity in a dynamic ocean model, *Global Biogeochem. Cycles*, *28*, 538–552, doi:10.1002/2013GB004704.

Nightingale, P. D., G. Malin, C. S. Law, A. J. Watson, P. S. Liss, M. I. Liddicoat, J. Boutin, and R. C. Upstill-Goddard (2000), In situ evaluation of air-sea gas exchange parameterizations using novel conservative and volatile tracers, *Global Biogeochem. Cycles*, *14*(1), 373–387.

Ohno, Y., N. Iwasaka, F. Kobashi, and Y. Sato (2009), Mixed layer depth climatology of the North Pacific, *Prog. Oceanogr.*, *65*, 1–16.

Ostle, C., M. Johnson, P. Landschützer, U. Schuster, S. Hartman, and C. Robinson (2014), Net community production in the North Atlantic Ocean derived from volunteer observing ship data, *Global Biogeochem. Cycles*, *29*, 80–95, doi:10.1002/2014GB004868.

Palevsky, H. I., F. Ribalet, J. E. Swalwell, C. E. Cosca, E. D. Cokelet, R. A. Feely, E. V. Armbrust, and P. D. Quay (2013), The influence of net community production and phytoplankton community structure on CO_2 uptake in the Gulf of Alaska, *Global Biogeochem. Cycles*, *27*, 664–676, doi:10.1002/gbc.20058.

Pelland, N. A. (2015), Eddy circulation, heat and salt balances and ocean metabolism: Observations from a seaglider-mooring array at Ocean Station Papa, PhD thesis, Univ. of Washington, Seattle.

Polovina, J. J., E. Howell, D. R. Kobayashi, and M. P. Seki (2001), The transition zone chlorophyll front, a dynamic global feature defining migration and forage habitat for marine resources, *Prog. Oceanogr.*, *49*, 469–483.

Prokopenko, M. G., O. M. Pauluis, J. Granger, and L. Y. Yeung (2011), Exact evaluation of gross photosynthetic production from the oxygen triple-isotope composition of O_2: Implications for the net-to-gross primary production ratios, *Geophys. Res. Lett.*, *38*, L14603, doi:10.1029/2011GL047652.

Quay, P. D., C. Peacock, K. Björkman, and D. M. Karl (2010), Measuring primary production rates in the ocean: Enigmatic results between incubation and non-incubation methods at Station ALOHA, *Global Biogeochem. Cycles*, *24*, GB3014, doi:10.1029/2009GB003665.

Quay, P., J. Stutsman, and T. Steinhoff (2012), Primary production and carbon export rates across the subpolar N. Atlantic Ocean basin based on triple oxygen isotope and dissolved O_2 and Ar gas measurements, *Global Biogeochem. Cycles*, *26*, GB2003, doi:10.1029/2010GB004003.

Redfield, A. C., B. H. Ketchum, and F. A. Richards (1963), The influence of organisms on the composition of seawater, in *The Sea*, vol. 2, edited by M. N. Hill, pp. 26–77, Interscience, New York.

Reuer, M. K., B. A. Barnett, M. L. Bender, P. G. Falkowski, and M. B. Hendricks (2007), New estimates of Southern Ocean biological production rates from O_2/Ar ratios and the triple isotope composition of O_2, *Deep Sea Res., Part I*, *54*, 951–974, doi:10.1016/j.dsr.2007.02.007.

Roden, G. I. (1991), Subarctic-subtropical transition zone of the North Pacific: Large-scale aspects and mesoscale structure, *NOAA Tech. Rep. NMFS*, *105*, 1–38.

Sasai, Y., K. J. Richards, A. Ishida, and H. Sasaki (2010), Effects of cyclonic mesoscale eddies on the marine ecosystem in the Kuroshio Extension region using an eddy-resolving coupled physical-biological model, *Ocean Dyn.*, *60*, 693–704, doi:10.1007/s10236-010-0264-8.

Shiomoto, A. (2000), Efficiency of water-column light utilization in the subarctic northwestern Pacific, *Limnol. Oceanogr.*, *45*(4), 982–987, doi:10.4319/lo.2000.45.4.0982.

Smayda, T. J. (1970), The suspension and sinking of phytoplankton in the sea, *Oceanogr. Mar. Biol. Ann. Rev.*, *8*, 353–414.

Sonnerup, R. E., S. Mecking, and J. L. Bullister (2013), Transit time distributions and oxygen utilization rates in the northeast Pacific Ocean from chlorofluorocarbons and sulfur hexafluoride, *Deep Sea Res., Part I*, *72*, 61–71, doi:10.1016/j.dsr.2012.10.013.

Stanley, R. H. R., J. B. Kirkpatrick, N. Cassar, B. A. Barnett, and M. L. Bender (2010), Net community production and gross primary production rates in the western equatorial Pacific, *Global Biogeochem. Cycles*, *24*, GB4001, doi:10.1029/2009GB003651.

Takahashi, T., et al. (2002), Global sea-air CO_2 flux based on climatological surface ocean pCO_2, and seasonal biological and temperature effects, *Deep Sea Res., Part II*, *49*, 1601–1622.

Takahashi, T., et al. (2009), Climatological mean and decadal change in surface ocean pCO_2, and net sea-air CO_2 flux over the global oceans, *Deep Sea Res., Part II*, *56*, 554–577, doi:10.1016/j.dsr2.2008.12.009.

Tsurushima, N., Y. Nojiri, K. Imai, and S. Watanabe (2002), Seasonal variations of carbon dioxide system and nutrients in the surface mixed layer at station KNOT (44°N, 155°E) in the subarctic western North Pacific, *Deep Sea Res., Part II*, *49*, 5377–5394, doi:10.1016/S0967-0645(02)00197-2.

Varela, D. E., and P. J. Harrison (1999), Seasonal variability in nitrogenous nutrition of phytoplankton assemblages in the northeastern subarctic Pacific Ocean, *Deep Sea Res., Part II*, *46*, 2505–2538, doi:10.1016/S0967-0645(99)00074-0.

Volk, T., and M. I. Hoffert (1985), Ocean carbon pumps: Analysis of relative strengths and efficiencies in ocean-driven atmospheric CO_2 changes, in *The Carbon Cycle and Atmospheric CO_2 Natural Variations Archean to Present*, vol. 32, edited by E. T. Sundquist and W. S. Broecker, pp. 99–110, AGU, Wahington, D. C.

Wanninkhof, R. (1992), Relationship between wind speed and gas exchange over the ocean, *J. Geophys. Res.*, *97*(C5), 7373–7382.

Welschmeyer, N. A., S. Strom, R. Goericke, G. DiTullio, M. Belvin, and W. Petersen (1993), Primary production in the subarctic Pacific Ocean: Project SUPER, *Prog. Oceanogr.*, *32*, 101–135, doi:10.1016/0079-6611(93)90010-B.

Wheeler, P. A. (1993), New production in the subarctic Pacific Ocean: Net changes in nitrate concentrations, rates of nitrate assimilation and accumulation of particulate nitrogen, *Prog. Oceanogr.*, *32*, 137–161, doi:10.1016/0079-6611(93)90011-2.

Wong, C. S., F. A. Whitney, K. Iseki, J. S. Page, and J. Zeng (1995), Analysis of trends in primary productivity and chlorophyll-a over two decades at Ocean Station P (50°N, 145°W) in the subarctic northeast Pacific Ocean, *Can. J. Fish. Aquat. Sci.*, *121*, 107–117.

Wong, C. S., N. A. D. Waser, Y. Nojiri, F. A. Whitney, J. S. Page, and J. Zeng (2002a), Seasonal cycles of nutrients and dissolved inorganic carbon at high and mid latitudes in the North Pacific Ocean during the Skaugran cruises: Determination of new production and nutrient uptake ratios, *Deep Sea Res., Part II*, *49*, 5317–5338.

Wong, C. S., N. A. D. Waser, F. A. Whitney, W. K. Johnson, and J. S. Page (2002b), Time-series study of the biogeochemistry of the north east subarctic Pacific: Reconciliation of the C_{org}/N remineralization and uptake ratios with the Redfield ratios, *Deep Sea Res., Part II*, *49*, 5717–5738, doi:10.1016/S0967-0645(02)00211-4.